


# Singlet-doublet fermionic dark matter and gravitational waves in a two-Higgs-doublet extension of the Standard Model

Basabendu Barman<sup>1,\*</sup>, Amit Dutta Banik<sup>2,†</sup> and Avik Paul<sup>3,‡</sup>

<sup>1</sup>*Department of Physics, Indian Institute of Technology Guwahati, Assam 781039, India*

<sup>2</sup>*Key Laboratory of Quark and Lepton Physics (MoE) and Institute of Particle Physics, Central China Normal University, Wuhan 430079, China*

<sup>3</sup>*Astroparticle Physics and Cosmology Division, Saha Institute of Nuclear Physics, HBNI, 1/AF Bidhannagar, Kolkata 700064, India*

 (Received 14 January 2020; accepted 21 February 2020; published 24 March 2020)

We present a study of singlet-doublet vectorlike leptonic dark matter (DM) in the framework of the two-Higgs-doublet model (2HDM), where the dark sector is comprised of one doublet and one singlet vectorlike fermion (VLF). The DM, that arises as an admixture of the neutral components of the VLFs, is stabilized by an imposed discrete symmetry  $\mathcal{Z}'_2$ . We test the viability of the DM candidate in the light of observations from Planck and recent limits on spin-independent direct detection experiments and search for its possible collider signals. In addition, we also look for the stochastic gravitational wave (GW) signatures resulting from strong first-order phase transition due to the presence of the second Higgs doublet. The model thus offers a viable parameter space for a stable DM candidate that can be probed from direct search, collider, and GW experiments.

DOI: [10.1103/PhysRevD.101.055028](https://doi.org/10.1103/PhysRevD.101.055028)

## I. INTRODUCTION

Despite strong evidence of the existence of dark matter (DM) from several astrophysical and cosmological observations like rotation curves of spiral galaxies [1,2], the bullet cluster [3], gravitational lensing [4], etc., the particle nature of DM is unknown to date. While Planck [5] results claim that nearly 26.5% of matter in the Universe is indeed DM, the Standard Model (SM) of particle physics is incapable of accounting for a viable DM candidate. Interestingly, if DM interactions with the SM particles are similar to those of electroweak interactions, and the particle DM has a mass around the electroweak scale, then such a DM can be thermally produced in the early Universe, followed by its freeze-out, leaving a thermal relic very close to the observed DM abundance ( $\Omega h^2 \sim 0.12$ ). This remarkable coincidence is often referred to as the weakly interacting massive particle (WIMP) miracle [6]. Although the WIMP remains as an elusive DM candidate (for a recent review on the status of WIMP, see [7]) as it

indicates a new physics signature around the TeV scale, the nonobservation of any excess both at the colliders and at the DM scattering experiments such as LUX [8], PandaX-II [9,10], and XENON1T [11,12], etc., compels us to strive for either an alternative to the WIMP paradigm [13–16] or to come up with some search strategies for DM detection other than the usual scattering experiments (for an overview, see [17]).

Motivated from these, in this work we propose a particle DM model by extending the SM with a second Higgs doublet and adding one vectorlike lepton doublet and one vectorlike lepton singlet. We consider a type-I two-Higgs-doublet model (2HDM), where one of the Higgs doublets is odd under a discrete  $\mathcal{Z}_2$  symmetry. Such an imposition of a discrete symmetry is very commonplace in context with 2HDM, as this necessarily prevents the appearance of tree-level flavor changing neutral current (FCNC) via Higgs [18–23]. The newly added fermions are assumed to be odd under a second  $\mathcal{Z}'_2$  symmetry. All the SM particles are even under both of the discrete symmetries  $\mathcal{Z}_2$  and  $\mathcal{Z}'_2$ . The imposition of two different discrete symmetries ensures a first-order phase transition (FOPT) without hampering the stability of the DM. Under these circumstances, the DM emerges as the lightest particle odd under  $\mathcal{Z}'_2$  due to an admixture of the neutral component of the doublet and the singlet. Studies of minimal singlet-doublet vectorlike DM in the SM has been exhaustively performed in the literature [24–42]. As is understandable, purely singlet vectorlike fermion (VLF) DM does not have any renormalizable

\*bb1988@iitg.ac.in

†amitdbanik@mail.ccnu.edu.cn

‡avik.paul@saha.ac.in

*Published by the American Physical Society under the terms of the Creative Commons Attribution 4.0 International license. Further distribution of this work must maintain attribution to the author(s) and the published article's title, journal citation, and DOI. Funded by SCOAP<sup>3</sup>.*

portal interaction with the SM to obtain the observed thermal relic abundance. The purely doublet VLF, on the other hand, annihilates too much to the SM due to its electroweak gauge interactions, thus making it underabundant unless the mass is  $\gtrsim \text{TeV}$ . A purely doublet VLF also faces stringent constraints from DM direct detection experiments because of the large scattering cross section mediated by the  $Z$  boson. In the present model, as we shall see, due to the presence of the second Higgs doublet, the bound from a direct search is less stringent. This is possible due to some destructive interference<sup>1</sup> between the scalar-mediated direct search diagrams. Even in the absence of such destructive interference, a small direct search cross section is still conceivable due to the suppression coming from the heavy Higgs mass and small scalar mixing. This provides some freedom of choosing a moderate  $\sin\theta$ . However, as the  $Z$ -mediated DM-nucleon scattering is still present, hence the constraint is not completely alleviated, and that confines the singlet-doublet mixing to some extent. This, in turn, affects the collider signature for this model. Here we would like to mention that our model is different from the one presented in Ref. [40], where the DM particles do not couple to the SM  $Z$  boson due to its Majorana nature.

The origin of the baryon asymmetry of the Universe (BAU) is another long-standing puzzle of particle physics. Electroweak baryogenesis (EWBG) is a possible way to account for the BAU exploiting the three Sakharov conditions [47]. However, it is not possible to have a successful EWBG within the SM paradigm, as the SM provides neither a sufficient  $CP$  violation nor a strong first-order phase transition (SFOPT) [48–51]. Therefore, a successful EWBG invokes new physics at the electroweak scale that can be obtained via an extended scalar sector. The 2HDM is a very well-motivated nonsupersymmetric extension of the SM, where the scalar sector of the SM is augmented with an additional Higgs doublet, giving rise to a plethora of different phenomenological implications [18–23,52–56]. In context with an electroweak phase transition (EWPT), the 2HDM has been extensively studied in both the  $CP$ -conserving case [57–59] and the  $CP$ -violating scenario [60–63]. It was also shown that the 2HDM framework is capable of generating a SFOPT [64,65].

The production of a gravitational wave (GW) spectrum happens mainly via three processes: bubble collisions [66–72], sound waves [73–76], and turbulence in the plasma [77–81]. The signal thus produced can be detected in different GW detectors, for example, space-based detectors like Advanced Laser Interferometer Antenna (ALIA) [82], Big Bang Observer (BBO) [83], Decihertz Interferometer Gravitational Wave Observatory (DECIGO) [84], Laser Interferometer Space Antenna (LISA) [85], ground-based detector advanced Laser Interferometer Gravitational-Wave

Observatory (aLIGO) [86], etc. The GW signature as a complementary search strategy in context with DM models has already been studied in the case of both freeze-out and freeze-in [67,87–94] (for a review on GW probes of DM, see [95]). We have shown, within a consistent framework, that our model is also capable of providing a detectable GW signal by satisfying all stringent DM, collider, and other theoretical constraints.

The paper is organized as follows: In Sec. II, we have introduced the particle content of the model along with the necessary interaction terms. In Sec. III, we have discussed the constraints on the model parameters arising due to tree-level unitarity, precision observables, and collider bounds. We next move on to Sec. IV, where we illustrate the parameter space satisfying relic abundance and direct detection bounds, from which we choose a couple of benchmark points to perform the collider analysis in Sec. V. Then in Sec. VI we detail the generation of a gravitational wave due to SFOPT and show the detector reach for this model. Finally, we conclude in Sec. VII.

## II. MODEL

### A. Fields and interactions

We extend the SM with the addition of a second Higgs doublet ( $\Phi_2$ ), along with two VLFs: one doublet  $\psi$  and one singlet  $\chi$ . In order to have a stable DM candidate, we need to impose a  $\mathcal{Z}'_2$  symmetry on the dark sector fermions, different from the existing  $\mathcal{Z}_2$  symmetry of the 2HDM, which is anyway required to forbid tree-level Higgs-mediated FCNC. A second discrete symmetry ( $\mathcal{Z}'_2$ ) is needed in this framework because of the presence of soft  $\mathcal{Z}_2$ -breaking term in the 2HDM scalar potential,<sup>2</sup> which can potentially lead to the decay of the DM to SM fermions if the DM is also stabilized under the same  $\mathcal{Z}_2$ . The  $\mathcal{Z}'_2$ , on the other hand, is exact. All SM fermions are even under both  $\mathcal{Z}_2$  and  $\mathcal{Z}'_2$ , which forbids the Yukawa interactions of the dark sector with the SM sector. Different charge assignments of new particles are listed in Table I.

In this setup, the Lagrangian for the model can be written as

$$\mathcal{L} = \mathcal{L}_{\text{SM}} + \mathcal{L}_f + \mathcal{L}_s + \mathcal{L}_{\text{yuk}}, \quad (1)$$

where  $\mathcal{L}_f$  is the Lagrangian for the VLFs,  $\mathcal{L}_s$  involves the SM doublet and the additional Higgs doublet, and  $\mathcal{L}_{\text{yuk}}$  contains the Yukawa interaction terms.

The interaction Lagrangian for the VLFs reads

$$\mathcal{L}_f = \bar{\psi} D \psi + \chi^{\dagger} \not{\partial} \chi - M_{\psi} \bar{\psi} \psi - M_{\chi} \chi^{\dagger} \chi, \quad (2)$$

where  $D_{\mu}$  is the covariant derivative under  $SU(2) \times U(1)$ :

<sup>1</sup>The presence of a “blind spot” in the direct search cross section for a 2HDM model has been studied in Refs. [40,43–46].

<sup>2</sup>The presence of these soft breaking terms has implications in ensuring decoupling behavior of the 2HDM.

TABLE I. New particle content of the model and their charge assignments.

Particles	$SU(3)_c$	$SU(2)$	$U(1)_Y$	$\mathcal{Z}_2$	$\mathcal{Z}'_2$
$\psi^T: (\psi^0, \psi^-)$	1	2	1	+	-
$\chi^0$	1	1	0	+	-
$\Phi_2$	1	2	1	+	+
$\Phi_1$	1	2	1	-	+

$$D_\mu \psi = \partial_\mu \psi - ig \frac{\sigma^a}{2} W_\mu^a \psi + i \frac{g'}{2} B_\mu \psi, \quad (3)$$

where  $g$  and  $g'$  are the gauge couplings corresponding to  $SU(2)$  and  $U(1)_Y$ , respectively, and  $a = 1, 2, 3$  are the indices for the generators of  $SU(2)$ .  $W_\mu$  and  $B_\mu$  are the gauge bosons corresponding to SM  $SU(2)$  and  $U(1)_Y$  gauge groups, respectively.

The Lagrangian of the scalar sector involving the SM Higgs doublet ( $H$ ) and the new Higgs doublet ( $\Phi_2$ ) can be written as

$$\mathcal{L}_s = (D^\mu \Phi_1)^\dagger (D_\mu \Phi_1) + (D^\mu \Phi_2)^\dagger (D_\mu \Phi_2) - V(\Phi_1, \Phi_2). \quad (4)$$

The model with such a modified scalar sector thus resembles the standard 2HDM of type I [18,20–22], where all SM fermions have Yukawa interactions with only one of the doublets, e.g.,  $\Phi_2$ . The most general renormalizable scalar potential can then be written as

$$\begin{aligned} V(\Phi_1, \Phi_2) = & m_{11}^2 \Phi_1^\dagger \Phi_1 + m_{22}^2 \Phi_2^\dagger \Phi_2 - m_{12}^2 (\Phi_1^\dagger \Phi_2 + \Phi_2^\dagger \Phi_1) \\ & + \frac{\lambda_1}{2} (\Phi_1^\dagger \Phi_1)^2 + \frac{\lambda_2}{2} (\Phi_2^\dagger \Phi_2)^2 + \lambda_3 \Phi_1^\dagger \Phi_1 \Phi_2^\dagger \Phi_2 \\ & + \lambda_4 \Phi_1^\dagger \Phi_2 \Phi_2^\dagger \Phi_1 + \frac{\lambda_5}{2} [(\Phi_1^\dagger \Phi_2)^2 + (\Phi_2^\dagger \Phi_1)^2]. \end{aligned} \quad (5)$$

As we shall see, the coefficient  $m_{12}$  of the softly  $\mathcal{Z}_2$ -breaking term plays the pivotal role in deciding the nature of the phase transition. Finally, the charge assignment allows us to write a Yukawa interaction [32,37,41]:

$$-\mathcal{L}_{\text{yuk}} = Y(\bar{\psi} \widetilde{\Phi}_2 \chi^0 + \text{H.c.}), \quad (6)$$

where  $Y$  is the Yukawa coupling between the VLFs and SM Higgs and  $\widetilde{\Phi}_2 = i\sigma_2 \Phi_2^*$ .

### B. Mixing in the scalar sector

We parametrize the scalar doublets as

$$\Phi_i = \begin{pmatrix} G_i^+ \\ \frac{h_i + v_i + iz_i}{\sqrt{2}} \end{pmatrix}, \quad (7)$$

for  $i = 1, 2$ . After spontaneous symmetry breaking, doublet Higgs fields acquire vacuum expectation values (VEVs)

$\langle \Phi_1 \rangle = v_1$  and  $\langle \Phi_2 \rangle = v_2$  such that  $\sqrt{v_1^2 + v_2^2} = v = 246$  GeV. The ratio of VEVs is given as  $\tan \beta = \frac{v_2}{v_1}$ . The physical states are obtained by diagonalizing the charged and neutral scalar mass matrices. There are then altogether eight mass eigenstates, three of which become the longitudinal components of the  $W^\pm$  and  $Z$  gauge bosons. Of the remaining five, there is one charged scalar  $H^\pm$ , two neutral  $CP$ -even scalars  $h$  and  $H$ , and one neutral pseudoscalar  $A$ . The mixing between  $CP$ -even scalars is denoted by an angle  $\alpha$ . For our analysis, we shall follow the *alignment limit* ( $\beta - \alpha = \frac{\pi}{2}$ ), under which  $h$  is recognized as the SM Higgs boson of mass 125.09 GeV [96] with exactly the same gauge, Yukawa, and self-couplings at tree level as those of the SM Higgs bosons, while  $H$  is the beyond SM (heavy) Higgs.

Different couplings occurring in the 2HDM scalar potential can be expressed in terms of physical masses  $\{m_h, m_H, m_{H^\pm}, m_A\}$ , mixings  $\{\alpha, \beta\}$ , VEV  $v$ , and  $m_{12}$ :

$$\lambda_1 = \frac{1}{v^2 c_\beta^2} \left( c_\alpha^2 m_H^2 + s_\alpha^2 m_h^2 - m_{12}^2 \frac{s_\beta}{c_\beta} \right), \quad (8)$$

$$\lambda_2 = \frac{1}{v^2 s_\beta^2} \left( s_\alpha^2 m_H^2 + c_\alpha^2 m_h^2 - m_{12}^2 \frac{c_\beta}{s_\beta} \right), \quad (9)$$

$$\lambda_4 = \frac{1}{v^2} (m_A^2 - 2m_{H^\pm}^2) + \frac{m_{12}^2}{v^2 s_\beta c_\beta}, \quad (10)$$

$$\lambda_5 = \frac{m_{12}^2}{v^2 s_\beta c_\beta} - \frac{m_A^2}{v^2}, \quad (11)$$

$$\lambda_3 = \frac{1}{v^2 s_\beta c_\beta} ((m_H^2 - m_h^2) s_\alpha c_\alpha + m_A^2 s_\beta c_\beta) - \lambda_4, \quad (12)$$

where we denote  $s_\alpha = \sin \alpha$  and  $c_\alpha = \cos \alpha$  and, similarly,  $s_\beta = \sin \beta$  and  $c_\beta = \cos \beta$ .

### C. Mixing in the VLF sector

After electroweak symmetry breaking, the neutral components of the doublet ( $\psi^0$ ) and singlet ( $\chi^0$ ) mix via the Yukawa interaction [Eq. (6)]. The mass matrix can be diagonalized in the usual way using a  $2 \times 2$  orthogonal rotation matrix to find the masses in the physical basis  $(\psi_1, \psi_2)^T$ :

$$\begin{pmatrix} m_{\psi_1} & 0 \\ 0 & m_{\psi_2} \end{pmatrix} = \mathcal{R}^T \begin{pmatrix} M_\psi & m \\ m & M_\chi \end{pmatrix} \mathcal{R}, \quad (13)$$

where the nondiagonal terms are present due to Eq. (6), and the rotation matrix is given by

$$\mathcal{R} = \begin{pmatrix} \cos \theta & \sin \theta \\ -\sin \theta & \cos \theta \end{pmatrix}.$$

The mixing angle is related to the masses in the weak (flavor) basis:

$$\tan 2\theta = \frac{2m}{M_\psi - M_\chi}. \quad (14)$$

The physical eigenstates (in the mass basis) are, therefore, a linear superposition of the neutral weak eigenstates. These can be expressed in terms of the mixing angles as

$$\psi_1 = \cos \theta \chi^0 + \sin \theta \psi^0, \quad \psi_2 = -\sin \theta \chi^0 + \cos \theta \psi^0. \quad (15)$$

The lightest electromagnetic charge neutral  $\mathcal{Z}_2$  odd particle is a viable DM candidate of this model. From now on, we shall refer  $\psi_1$  as the lightest stable particle of the model. In the small mixing limit, the charged component of the VLF doublet  $\psi^\pm$  acquires a mass as

$$m_{\psi^\pm} = m_{\psi_1} \sin^2 \theta + m_{\psi_2} \cos^2 \theta \approx m_{\psi_2}. \quad (16)$$

From Eq. (14), we see that the VLF Yukawa is related to the mass difference between two physical eigenstates and is no more an independent parameter:

$$Y = \frac{(m_{\psi_2} - m_{\psi_1}) \sin 2\theta \cot \beta}{\sqrt{2}v_1} = \frac{\Delta m \sin 2\theta \cot \beta}{\sqrt{2}v_1}. \quad (17)$$

Therefore, one can have three new parameters:  $\{m_{\psi_1}, \Delta m, \sin \theta\}$  from DM phenomenology apart from 2HDM parameters. These three parameters will play the key role in determining the relic abundance of the DM, also deciding the fate of the model in direct and collider searches.

### III. CONSTRAINTS ON THE MODEL PARAMETERS

In this section, we would like to summarize constraints on the masses, mixings, and couplings arising in the model due to theoretical and experimental bounds. We are particularly interested in the choice of  $\tan \beta$  and heavy scalar masses in the 2HDM sector in order to have a SFOPT, while the free parameters appearing in the VLF sector are mostly constrained by oblique parameters and later from DM phenomenology.

#### A. Vacuum stability

Stability of the 2HDM potential is ensured by the following conditions [21,22,97]:

$$\begin{aligned} \lambda_1, \lambda_2 > 0; \quad \lambda_3 + 2\sqrt{\lambda_1 \lambda_2} > 0; \\ \lambda_3 + \lambda_4 - |\lambda_5| + 2\sqrt{\lambda_1 \lambda_2} > 0. \end{aligned} \quad (18)$$

These conditions have been shown to be necessary and sufficient [98] to ensure that the scalar potential is bounded from below [99].

#### B. Perturbativity

Tree-level unitarity imposes bounds on the size of the quartic couplings  $\lambda_i$  or various combinations of them. The quartic couplings and the Yukawa couplings appearing in the theory need to satisfy [21,22,97]

$$|\lambda_i| < 4\pi, \quad |Y| < \sqrt{4\pi}, \quad (19)$$

in order to remain within the perturbative limit. Here  $\lambda_i = \lambda, \lambda_{1,2,3,4,5}$ . Here we would like to mention that absolute stability of the vacuum at tree level puts a bound on  $\tan \beta$  depending on the choice of  $m_H$  as derived in Ref. [100]. For  $m_H \simeq 300\text{--}400$  GeV, this typically allows  $1 \lesssim \tan \beta \lesssim 30$ . However, as has been discussed in Refs. [101–104], for  $1 \leq \tan \beta \leq 5$ , the quartic couplings are within the perturbativity bound, and tree-level unitarity is also satisfied.

#### C. Constraints from phase transition

In Refs. [57,64,65,104], a detailed study of a phase transition in context with the 2HDM has been done, and, hence, we do not repeat it here; rather, our aim is to see whether our DM parameter space is in agreement with the choice of the parameters of the scalar potential that can trigger a SFOPT giving rise to a measurable GW signal. It is possible to have a SFOPT in the 2HDM for  $m_{H^\pm} \simeq m_A \approx 600$  GeV and a large positive mass difference between  $m_{H^\pm}$  and  $m_H$ :  $m_{H^\pm} - m_H \gtrsim 300$  GeV [64,65] with  $\tan \beta \sim 1$  [104]. In our entire analysis, we thus keep  $m_{H^\pm} = m_A = 650$  GeV and  $m_H = 300$  GeV for two different choices of  $\tan \beta = 1.3$  and  $\tan \beta = 5$ . Such choices of the  $\tan \beta$  is in agreement with the DM phenomenology. As discussed in Refs. [64,104], a SFOPT can take place in a type-I 2HDM even if the masses of the three extra Higgs bosons are degenerate  $\sim 350$  GeV. Such a scenario leads to a potentially testable premise through the  $A \rightarrow Hh$  decay channel at colliders.

#### D. Electroweak precision observables (EWPOs)

The splitting between the heavy scalar masses is constrained by the oblique electroweak  $T$  parameter whose expression in the alignment limit is given by [21,97,105–107]

$$\Delta T = \frac{g^2}{64\pi^2 m_W^2} (\xi(m_{H^\pm}^2, m_A^2) + \xi(m_{H^\pm}^2, m_H^2) - \xi(m_A^2, m_H^2)), \quad (20)$$

with

$$\xi(x, y) = \begin{cases} \frac{x+y}{2} - \frac{xy}{x-y} \ln\left(\frac{x}{y}\right), & \text{if } x \neq y, \\ 0, & \text{if } x = y. \end{cases} \quad (21)$$

As Eq. (21) suggests, this new physics contribution to the  $T$  parameter vanishes in the limit  $m_{H^\pm} = m_A$  or  $m_{H^\pm} = m_H$ . Since we are working in the exact alignment limit and a SFOPT demands  $m_{H^\pm} = m_A$  [64], a  $T$  parameter puts no bound on the scalar sector in our setup. The presence of the new VLFs shall also contribute to the  $T$  parameter [108]:

$$T^{\text{VLF}} = \frac{g^2}{16\pi m_W^2} (-2\sin^2\theta\Pi(M_\psi, m_{\psi_1})) - \frac{g^2}{16\pi m_W^2} (2\cos^2\theta\Pi(M_\psi, m_{\psi_2})) + \frac{g^2}{16\pi m_W^2} (2\cos^2\theta\sin^2\theta\Pi(m_{\psi_1}, m_{\psi_2})), \quad (22)$$

where

$$\begin{aligned} \Pi(m_i, m_j) = & -\frac{1}{2}(m_i^2 + m_j^2) \left( \text{div} + \log\left(\frac{\mu_{EW}^2}{m_i m_j}\right) \right) \\ & + m_i m_j \left( \text{div} + \frac{(m_i^2 + m_j^2) \log\left(\frac{m_i^2}{m_j^2}\right)}{2(m_i^2 - m_j^2)} \right) \\ & + \log\left(\frac{\mu_{EW}^2}{m_i m_j}\right) + 1 \\ & - \frac{1}{4}(m_i^2 + m_j^2) - \frac{(m_i^4 + m_j^4) \log\left(\frac{m_j^2}{m_i^2}\right)}{4(m_i^2 - m_j^2)}. \end{aligned} \quad (23)$$

The bound on  $\hat{S}$  comes from a global fit:  $10^3 \hat{S} = 0.0 \pm 1.3$  [109]. For the  $S$  parameter, we consider a contribution only due to the VLFs as given by [37,42,108]

$$\begin{aligned} \hat{S} = & \frac{g^2}{16\pi^2} (\tilde{\Pi}'(m_{\psi^\pm}, m_{\psi^\pm}, 0) - \cos^4\theta\tilde{\Pi}'(m_{\psi_1}, m_{\psi_1}, 0) \\ & - \sin^4\theta\tilde{\Pi}'(m_{\psi_2}, m_{\psi_2}, 0)) \\ & - \frac{g^2}{16\pi^2} (2\sin^2\theta\cos^2\theta\tilde{\Pi}'(m_{\psi_2}, m_{\psi_1}, 0)), \end{aligned} \quad (24)$$

where  $g_2$  is the  $SU(2)_L$  gauge coupling. The expression for vacuum polarization for identical masses (at  $q^2 = 0$ ) [37,42,108] is

$$\tilde{\Pi}'(m_i, m_i, 0) = \frac{1}{3} \text{div} + \frac{1}{3} \ln\left(\frac{\mu_{EW}^2}{m_i^2}\right). \quad (25)$$

For two different masses ( $m_i \neq m_j$ ), the expression for vacuum polarization reads [37,42,108]

$$\begin{aligned} \tilde{\Pi}'(m_i, m_j, 0) = & \left( \frac{1}{3} \text{div} + \frac{1}{3} \ln\left(\frac{\mu_{EW}^2}{m_i m_j}\right) \right) + \frac{m_i^4 - 8m_i^2 m_j^2 + m_j^4}{9(m_i^2 - m_j^2)^2} \\ & + \frac{(m_i^2 + m_j^2)(m_i^4 - 4m_i^2 m_j^2 + m_j^4)}{6(m_i^2 - m_j^2)^3} \ln\left(\frac{m_j^2}{m_i^2}\right) \\ & + m_i m_j \left( \frac{1}{2} \frac{m_i^2 + m_j^2}{(m_i^2 - m_j^2)^2} + \frac{m_i^2 m_j^2}{(m_i^2 - m_j^2)^3} \ln\left(\frac{m_j^2}{m_i^2}\right) \right). \end{aligned} \quad (26)$$

Note that all the divergences appearing in Eqs. (25) and (26), along with the renormalization scale  $\mu_{EW}$ , are canceled on substitution in Eq. (24). In the lhs of Fig. 1, we have shown the region allowed by the bound on the  $T$  parameter in the bidimensional plane of  $m_{\psi_1} - \Delta m$ . We see that large  $\Delta m$  is compatible with the  $T$  parameter for small

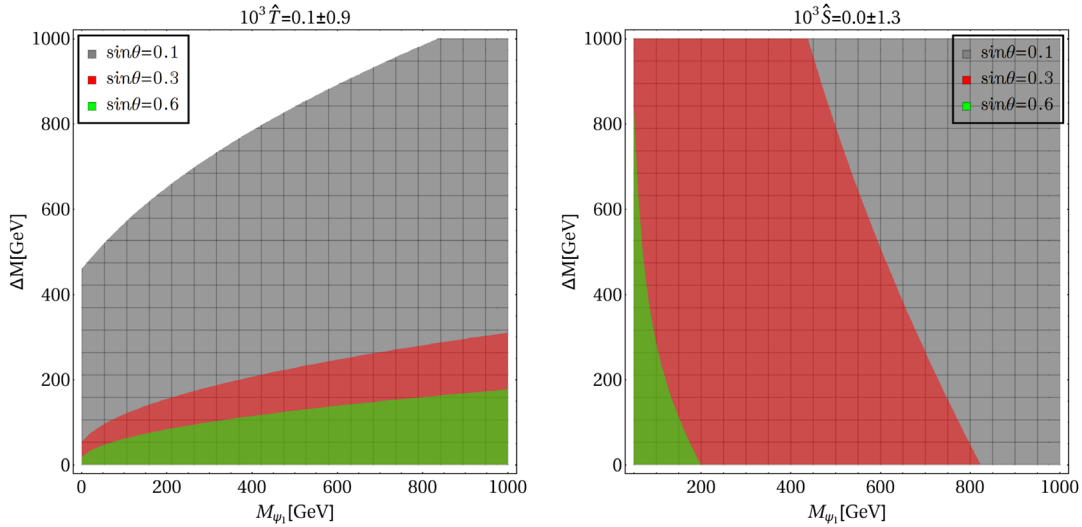


FIG. 1. Left: Limit from  $\hat{T}$  on DM mass  $m_{\psi_1}$  and  $\Delta m$  for different choices of  $\sin\theta$ :  $\{0.1, 0.3, 0.6\}$  shown, respectively, in gray, red, and green. Right: Limit from  $\hat{S}$  on DM mass  $m_{\psi_1}$  and  $\Delta m$  for different choices of  $\sin\theta$ :  $\{0.1, 0.3, 0.6\}$  shown, respectively, in gray, red, and green.

$\sin \theta$ , while large  $\sin \theta$  heavily constrains  $\Delta m \lesssim 300$  GeV irrespective of the DM mass. The bound is rather complementary in the case of the  $S$  parameter as depicted in the rhs of Fig. 1. Here we see large  $\sin \theta$  constrains the DM mass  $\lesssim 200$  GeV, but  $\Delta m$  is allowed up to 1 TeV for any choice of the VLF mixing.

### E. Collider bounds

The LEP experiments have performed direct searches for charged Higgs. A combination of LEP data from searches in the  $\tau\nu$  and  $cs$  final states put a limit of  $m_{H^\pm} \gtrsim 80$  GeV [110,111] under the assumption that the decay  $H^\pm \rightarrow W^\pm h_1$  is absent. If the aforementioned decay channel is open, then DELPHI and OPAL provide complementary constraints that slightly weaken the charged Higgs mass:  $m_{H^\pm} \gtrsim 72.5$  GeV [110,111] for type-I 2HDM (in the context of LEP searches, Ref. [112] is also relevant). Moving on to LHC constraints which come from the  $t \rightarrow H^\pm b$  search with  $H^\pm \rightarrow \tau\nu$  or  $cs$  final states [113–116], the values of the charged Higgs masses for which such decay is kinematically allowed are excluded for  $\tan \beta \lesssim 10$  [40] in type-I 2HDM. Here we would like to mention that in type-I 2HDM  $\tan \beta$  is unconstrained from Higgs signal strength in the strict alignment limit, that otherwise puts a strong limit [40,117–119]. Flavor physics observables provide very strong constraints on the charged Higgs mass. Inclusive  $b \rightarrow s\gamma$  and more general  $b \rightarrow s$  transitions lead to a robust exclusion of  $m_{H^\pm} < 570$  GeV [120] for type-II 2HDM, while for type I it is excluded for  $\tan \beta \gtrsim 2$  [111]. For type-I 2HDM, the constraint from meson decay is rather weak, allowing  $m_{H^\pm} \gtrsim 200$  GeV for  $\tan \beta \sim 1.5$  [121,122].

Finally, we would like to highlight that LEP has set a lower limit on pair-produced charged heavy vectorlike leptons:  $m_\psi \gtrsim 101.2$  GeV at 95% C.L. for  $\psi^\pm \rightarrow \nu W^\pm$  final states [123]. For a  $SU(2)_L$  singlet charged vectorlike lepton, the CMS search does not improve on the LEP limits. The limits for a heavy lepton doublet decaying to  $\ell \in \{e, \mu\}$  flavors are  $m_L \gtrsim 450$  GeV [124]. In the case of decays to the  $\tau$  flavor, the limits are less stringent:  $m_L \gtrsim 270$  GeV [124]. However, in our case the charged VLF  $\psi^\pm$  has dominant decay to the DM  $\psi_1$ . As a result, the limits are less stringent, and we follow only the LEP limit in choosing our benchmark points for all the analyses.

### F. Invisible decay constraints

When the DM mass  $m_{\psi_1} < m_{h_1}/2$  or  $m_{\psi_1} < m_Z/2$ , they can decay to a pair of the VLF DM ( $\psi_1$ ). Higgs and  $Z$  invisible decays are precisely measured at the LHC [96]. Our model thus can be constrained from these measurements in the low mass range of DM. Both the Higgs and  $Z$  invisible decays to DM are proportional to VLF mixing angle  $\sin \theta$ . In the Appendix, Sec. 1, we have computed the invisible decay width of the Higgs and  $Z$  boson.

## IV. DARK MATTER PHENOMENOLOGY

In this section, we would like to elaborate on the DM phenomenology, where we show in detail the parameter space satisfying the Planck observed relic density by scanning over the free parameters of the model. Then we investigate how much of the relic density allowed parameter space also satisfies current direct detection bounds, e.g., from XENON1T [11,12]. Finally, from the resulting parameter space satisfying relic abundance, direct search, and existing theoretical and experimental bounds discussed earlier, we choose a few benchmark points for further analysis. All the relevant Feynman diagrams that contribute to the DM freeze-out are listed in the Appendix, Sec. 2 (Figs. 11–13).

### A. Relic abundance of the dark matter

As we have already mentioned earlier,  $\psi_1$  is the lightest VLF physical eigenstate which is odd under  $\mathcal{Z}_2$  and, hence, a potential DM candidate in this model. The relic abundance of  $\psi_1$  is mainly governed by the DM number changing annihilation and coannihilation processes mediated by the SM Higgs  $h_1$ , the nonstandard Higgses  $h_2$  and  $h_3$ , and the SM gauge bosons  $Z$  and  $\gamma$  to various SM final states. The DM number density, thus, can be determined by solving the Boltzmann equation [6,125] for single-component DM, which in our case reads

$$\frac{dn}{dt} + 3Hn = -\langle \sigma v \rangle_{\text{eff}} (n^2 - n_{\text{eq}}^2), \quad (27)$$

where

$$\begin{aligned} \langle \sigma v \rangle_{\text{eff}} = & \frac{g_1^2}{g_{\text{eff}}^2} \langle \sigma v \rangle_{\bar{\psi}_1 \psi_1} \\ & + \frac{2g_1 g_2}{g_{\text{eff}}^2} \langle \sigma v \rangle_{\bar{\psi}_1 \psi_2} \left( 1 + \frac{\Delta m}{m_{\psi_1}} \right)^{3/2} e^{-x(\Delta m/m_{\psi_1})} \\ & + \frac{2g_1 g_3}{g_{\text{eff}}^2} \langle \sigma v \rangle_{\bar{\psi}_1 \psi^-} \left( 1 + \frac{\Delta m}{m_{\psi_1}} \right)^{3/2} e^{-x(\Delta m/m_{\psi_1})} \\ & + \frac{2g_2 g_3}{g_{\text{eff}}^2} \langle \sigma v \rangle_{\bar{\psi}_2 \psi^-} \left( 1 + \frac{\Delta m}{m_{\psi_1}} \right)^3 e^{-2x(\Delta m/m_{\psi_1})} \\ & + \frac{g_2^2}{g_{\text{eff}}^2} \langle \sigma v \rangle_{\bar{\psi}_2 \psi_2} \left( 1 + \frac{\Delta m}{m_{\psi_1}} \right)^3 e^{-2x(\Delta m/m_{\psi_1})} \\ & + \frac{g_3^2}{g_{\text{eff}}^2} \langle \sigma v \rangle_{\psi^+ \psi^-} \left( 1 + \frac{\Delta m}{m_{\psi_1}} \right)^3 e^{-2x(\Delta m/m_{\psi_1})}, \quad (28) \end{aligned}$$

with  $n = n_{\psi_1} + n_{\psi_2} + n_{\psi^\pm}$  and  $H$  is the Hubble parameter. In the above equation,  $g_{\text{eff}}$  is defined as effective degrees of freedom, given by

$$\begin{aligned} g_{\text{eff}} = & g_1 + g_2 \left( 1 + \frac{\Delta m}{m_{\psi_1}} \right)^{3/2} e^{-x(\Delta m/m_{\psi_1})} \\ & + g_3 \left( 1 + \frac{\Delta m}{m_{\psi_1}} \right)^{3/2} e^{-x(\Delta m/m_{\psi_1})}, \quad (29) \end{aligned}$$

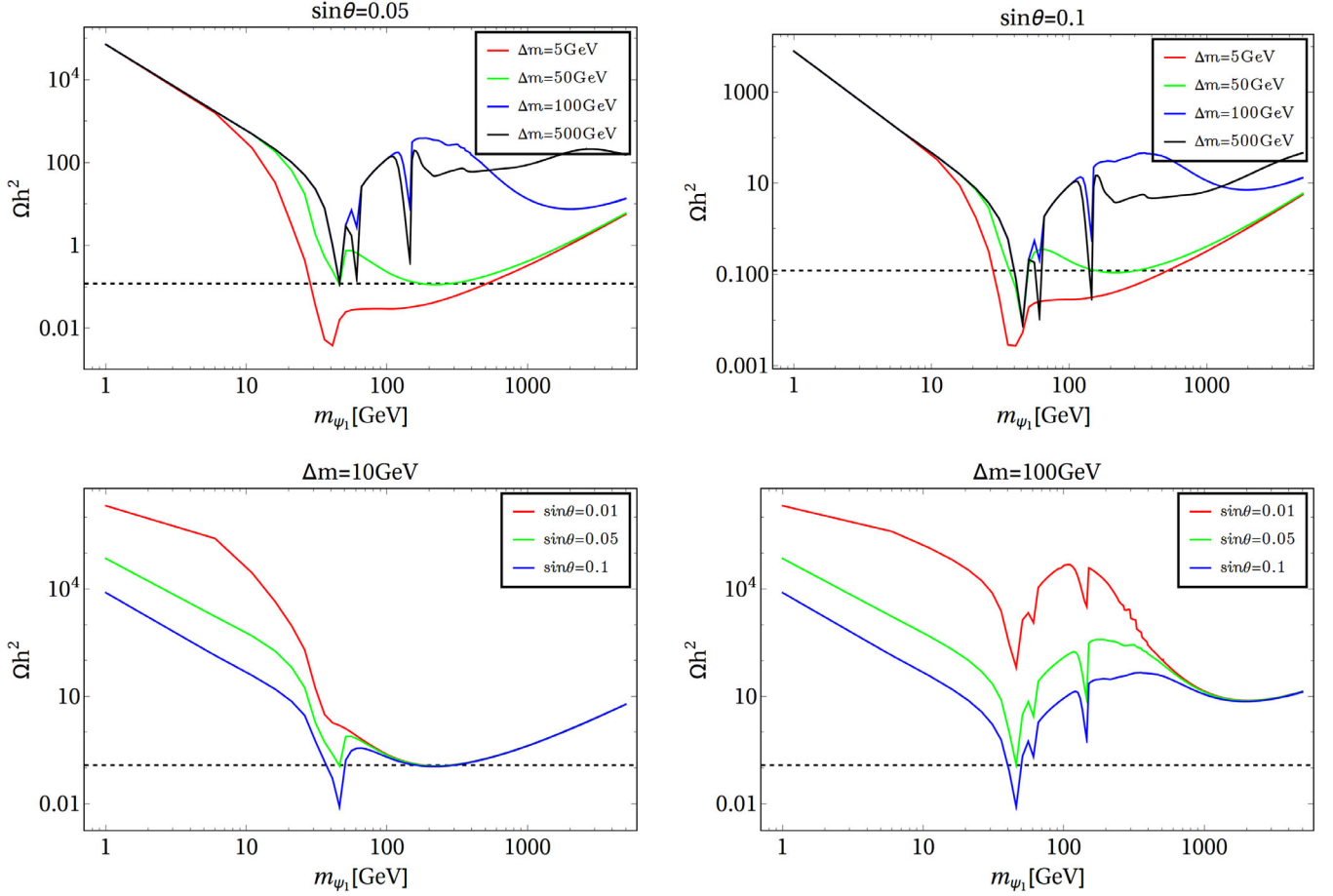


FIG. 2. Top left: Variation of relic abundance with DM mass for  $\Delta m$ :  $\{5, 50, 100, 500\}$  GeV in red, green, blue, and black, respectively, for VLF mixing  $\sin \theta = 0.05$ . Top right: The same with  $\sin \theta = 0.1$ . Bottom left: Variation of DM relic abundance with  $m_{\psi_1}$  for different choices of  $\sin \theta$ :  $\{0.01, 0.05, 0.1\}$  shown in red, green, and blue, respectively, for a fixed  $\Delta m = 10$  GeV. Bottom right: The same for  $\Delta m = 100$  GeV. For all plots,  $\tan \beta = 1.3$  has been chosen with  $m_{12} = 170$ .

where  $g_1$ ,  $g_2$ , and  $g_3$  are the degrees of freedom of  $\psi_1$ ,  $\psi_2$ , and  $\psi^\pm$ , respectively, and  $x = x_f = \frac{m_{\psi_1}}{T_f}$ , where  $T_f$  is the freeze-out temperature. We have implemented the model in LanHEP-3.3.2 [126], and the model files are then fed into micrOMEGAS-4.3.5 [127] for determining the relic abundance and direct detection cross section for the DM. Before delving into the detailed parameter scan, we first start by looking into the variation of relic density with DM mass  $m_{\psi_1}$  for some fixed choices of two of the other free parameters:  $\{\Delta m, \sin \theta\}$ . Here we would like to clarify that for the entire analysis we have kept the masses of the new scalars fixed at

$$m_H = 300 \text{ GeV}; \quad m_{H^\pm} = m_A = 650 \text{ GeV}. \quad (30)$$

We perform a scan over a range of the parameter space:

$$\begin{aligned} m_{\psi_1} : \{1-3000\} \text{ GeV}; & \quad \Delta m : \{1-3000\} \text{ GeV}; \\ \sin \theta : \{0.01-0.8\}; & \\ m_{12} : \{1-500\} \text{ GeV}. & \end{aligned} \quad (31)$$

As discussed earlier in Sec. III C, this choice of the scalar masses is motivated from the requirement of a SFOPT. Also, we would like to remind once more that we are strictly following the alignment limit, and, hence, the lightest  $CP$ -even scalar resembles the 125 GeV observed Higgs.

In Fig. 2, we show how the relic density of the DM  $\psi_1$  varies with the DM mass while we choose some of the free parameters at fixed values. In the left-hand side (lhs) of the top panel, we show such a variation for a fixed VLF mixing  $\sin \theta = 0.05$  for four different values of  $\Delta m$ :  $\{5, 50, 100, 500\}$  GeV in red, green, blue, and black curves, respectively. Here we see a number of interesting features. First of all, for smaller  $\Delta m$  (red), the DM is largely underabundant. This is due to the fact that smaller  $\Delta m$  enhances coannihilation by making the effective annihilation cross section large as evident from Eq. (28). This, in turn, reduces the relic abundance. For larger  $\Delta m$ , the coannihilation effect diminishes, and we see the right relic is obtained at two sharp resonances:  $m_{\psi_1} = \frac{m_Z}{2}$  and  $m_{\psi_1} = \frac{m_h}{2}$ . There is another resonance at  $m_{\psi_1} \simeq 150$  GeV,

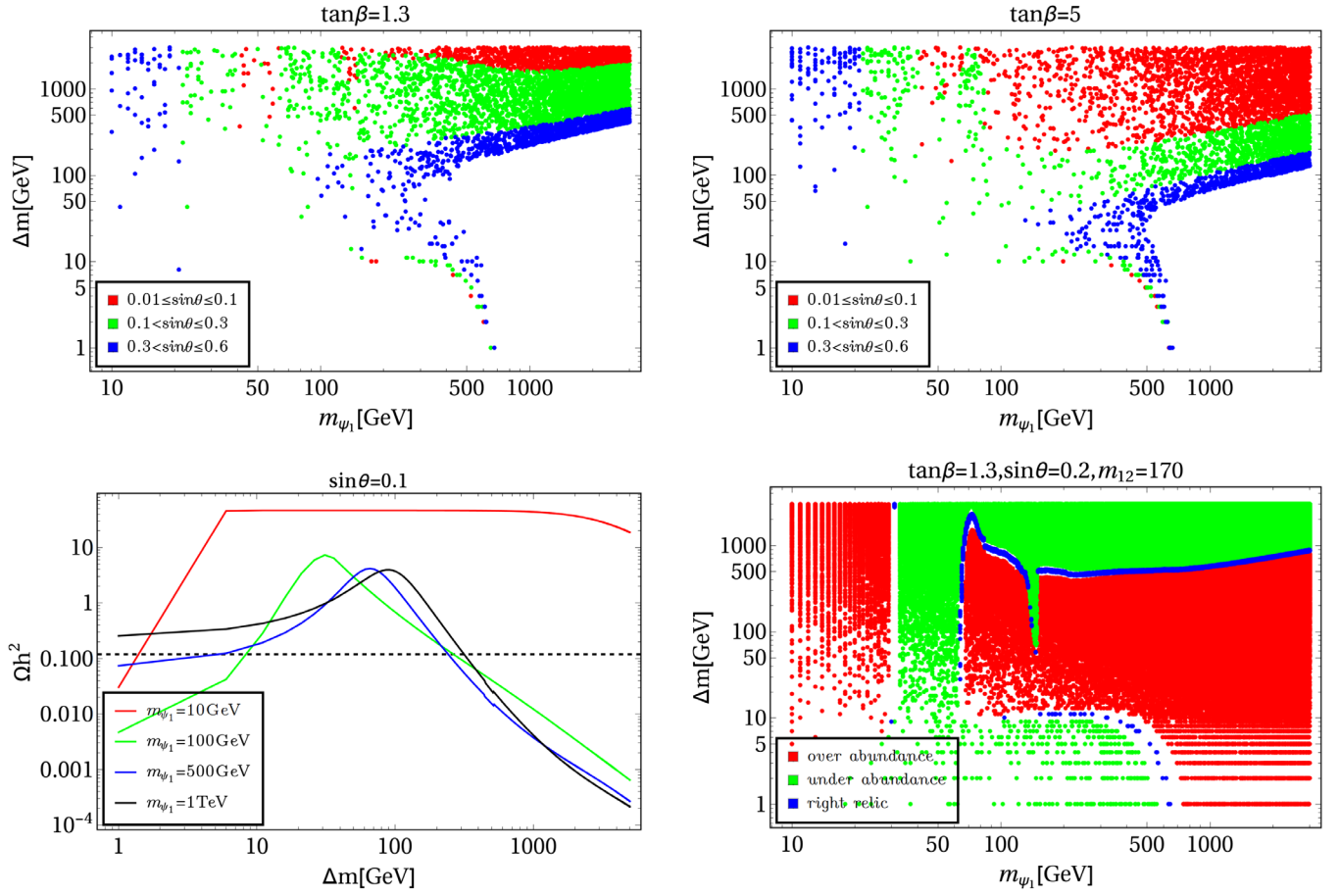


FIG. 3. Top left: Parameter space satisfying Planck observed relic abundance in the  $m_{\psi_1}$ - $\Delta m$  plane for  $0.01 \leq \sin\theta \leq 0.1$  in red,  $0.1 < \sin\theta \leq 0.3$  in green, and  $0.3 < \sin\theta \leq 0.6$  in blue, respectively, for  $\tan\beta = 1.3$ . Top right: The same for  $\tan\beta = 5$  (color codes are unchanged). In both cases, the gray shaded region below represents the neutrino floor (see the text for details). Bottom left: Variation of DM relic abundance with  $\Delta m$  for a fixed  $\sin\theta = 0.1$  and four different choices of the DM mass:  $m_{\psi_1} : \{10, 100, 500, 1000\}$  GeV. Bottom right: Parameter space in the  $m_{\psi_1}$ - $\Delta m$  plane for a fixed  $\sin\theta = 0.1$ , where the overabundant, underabundant, and observed abundant regions are shown, respectively, in red, green, and blue.

which occurs due to the second Higgs at 300 GeV. Thus, for a fixed  $\sin\theta$ , smaller  $\Delta m \simeq 5$  GeV results in coannihilation dominantly to light quark final states. For larger  $\Delta m \simeq 100$  GeV, on the other hand, annihilation dominates, and  $WW, Zh_1, h_1h_1$  final states contribute dominantly to the relic abundance. We see the same features in the right-hand side (rhs) of the top panel in Fig. 2. In both the plots, all the curves rise with the increase in DM mass, ensuring the unitarity of the model. In the bottom panel in Fig. 2, we again show the variation of relic density of the DM with DM mass  $m_{\psi_1}$ , but now for a fixed  $\Delta m$  and for three different  $\sin\theta$ :  $\{0.01, 0.05, 0.1\}$  in red, green, and blue, respectively. Here we see, again, for small  $\Delta m$  (left-hand side of the bottom panel), due to coannihilation domination, the resonances are not sharp. However, with an increase in  $\sin\theta$ , the DM becomes underabundant. This is understandable, as larger  $\sin\theta$  gives rise to larger (co) annihilation due to  $\sin^2\theta$  dependence at the vertex for gauge-mediated processes and  $\sin 2\theta$  dependence for

scalar-mediated processes (due to proportionality to the Yukawa  $Y$ ). As a result, the relic abundance naturally decreases. On the rhs in the bottom panel in Fig. 2, we show the same plot as that of the lhs but for larger  $\Delta m = 100$  GeV. Now we see, as before, the resonances become important where the observed relic density is achieved. For all these plots, we have kept  $\tan\beta = 1.3$  and  $m_{12} = 170$ ; for some other choice of  $\tan\beta$  (e.g.,  $\tan\beta = 5$ ), the inferences remain unaltered.

In the top left panel in Fig. 3, we show the parameter space allowed by the Planck observed relic density in the  $m_{\psi_1}$ - $\Delta m$  plane for different choices of the VLF mixing  $\sin\theta$ , where  $0.01 \leq \sin\theta \leq 0.1$  is shown by the red points,  $0.1 < \sin\theta \leq 0.3$  are shown by the green points, and  $0.3 < \sin\theta \leq 0.6$  where  $\tan\beta = 1.3$ . Here we see, large  $\Delta m$  is achieved for smaller  $\sin\theta$ . This can be intuitively understood in the following way: The scalar-mediated annihilation channels are essentially proportional to the Yukawa  $Y$ , which is proportional to both  $\sin\theta$  and  $\Delta m$ . Hence, a



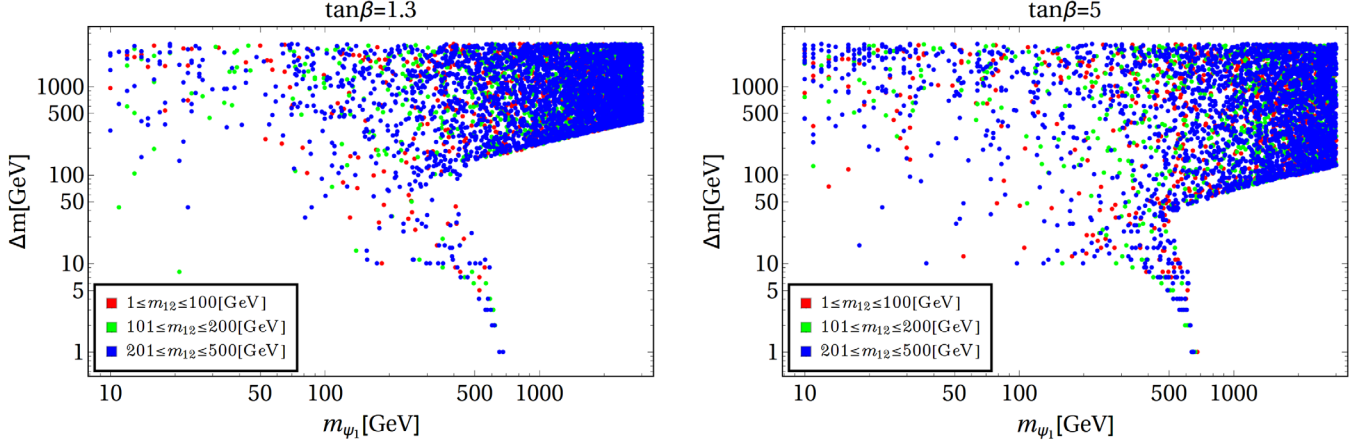


FIG. 4. Left: Relic density allowed parameter space in the bidimensional plane of  $m_{\psi_1} - \Delta m$ , where different colors correspond to different choices of  $m_{12}$ :  $1 \leq m_{12} \leq 100$  GeV in red,  $101 < m_{12} \leq 200$  GeV in green, and  $201 \leq m_{12} \leq 300$  GeV in blue for  $\tan\beta = 1.3$ . Right: The same for  $\tan\beta = 5$ .

smaller  $\sin\theta$  requires a larger  $\Delta m$  to produce the correct abundance. On the top right panel in Fig. 3, the same parameter space is shown for  $\tan\beta = 5$ . We note the same pattern here except for the fact that the  $0.01 \leq \sin\theta \leq 0.1$  region is more populated. This is a direct consequence of Eq. (17), which shows  $\sin\theta$  needs to be reduced as  $\tan\beta$  increases (i.e.,  $v_2$  increases) to adjust the Yukawa  $Y$  such that the relic abundance is satisfied.

In order to understand the behavior more intricately, we have obtained a parameter space for a fixed  $\sin\theta$  in the  $m_{\psi_1} - \Delta m$  plane as shown in the bottom right panel in Fig. 3. Here we have shown three different regions corresponding to underabundance (green), overabundance (red), and the right relic (blue). As we move from left to right in this plot, we first encounter overabundant regions for small DM mass  $\lesssim 20$  GeV. This is due to the lack of annihilation channels present for the DM to produce the right relic, as the only annihilation channels are to the light quarks. As we reach  $m_{\psi_1} \sim 30$  GeV, coannihilation starts playing, and, as a consequence, the DM becomes underabundant. Still, the right relic abundance is not obtained, as  $Y$  is small due to small  $\Delta m$ , and, hence, all the scalar-mediated annihilations do not contribute significantly. The right relic is first obtained at  $m_{\psi_1} \sim \frac{m_{h_1}}{2}$ , due to the SM Higgs resonance. For DM mass  $\sim 100$  GeV as we move from lower  $\Delta m$  to higher  $\Delta m$  (from bottom to top), the DM is at first underabundant due to coannihilation domination. Then the right relic abundance is achieved as the coannihilation is correctly tuned. Immediately after that, there is an overabundant region for larger  $\Delta m$  as coannihilation loses its goodness, and, hence, the effective annihilation cross section [Eq. (28)] becomes small. Note that, for a fixed DM mass  $\gtrsim 100$  GeV, the right relic abundance is reached twice: (a) once for small  $\Delta m$ , where the right coannihilation gives rise to the observed relic, and (b) for large  $\Delta m$ , where  $Y$  is large enough to produce the correct relic via scalar-mediated

channels (to gauge-boson-dominated final states) as shown in the bottom left panel in Fig. 3. Beyond  $m_{\psi_1} \sim 500$  GeV, the parameter space is largely overabundant as the suppression due to  $1/m_{\psi_1}^2$  becomes significant, thus overproducing the DM. Note that the right relic abundance is also obtained at the second Higgs resonance at  $m_{\psi_1} \sim 150$  GeV. Beyond  $\Delta m \sim 200$  GeV, for a fixed DM mass, the parameter space is largely underabundant as coannihilation is completely switched off and annihilation to all possible final states are open. This produces a very large effective annihilation cross section, making the DM completely underabundant. A cumulative effect of all these features is reflected in the upper panel in Fig. 3 for different choices of the VLF mixing  $\sin\theta$ . Before moving on to the DM direct search section, we would like to see what the values of  $m_{12}$  are that satisfy the right relic abundance. This is shown in Fig. 4 for both  $\tan\beta = 1.3$  (left) and  $\tan\beta = 5$  (right). As we see, the dependence of the relic abundance parameter space on the choice  $m_{12}$  is not very strict, as almost all values of  $m_{12}$  are allowed by any choice of DM mass and  $\Delta m$ .

## B. Direct detection of the dark matter

In the present framework, the DM exhibits spin-independent interactions with the nuclei induced at the tree level by the mediation of  $CP$ -even states  $h_1$  (SM Higgs-like) and  $h_2$  (heavier Higgs) and also by the SM  $Z$ -boson exchange (as in Fig. 5). The relevant cross section per nucleon reads [40]

$$\sigma_{SI}^{h_{1,2}} = \frac{1}{\pi A^2} \mu_r^2 \|\mathcal{M}\|^2, \quad (32)$$

where  $A$  is the mass number of the target nucleus,  $\mu_r = \frac{m_{\psi_1} m_N}{m_{\psi_1} + m_N}$  is the DM-nucleus reduced mass, and  $\|\mathcal{M}\|$  is the spin-averaged DM-nucleus scattering amplitude given by

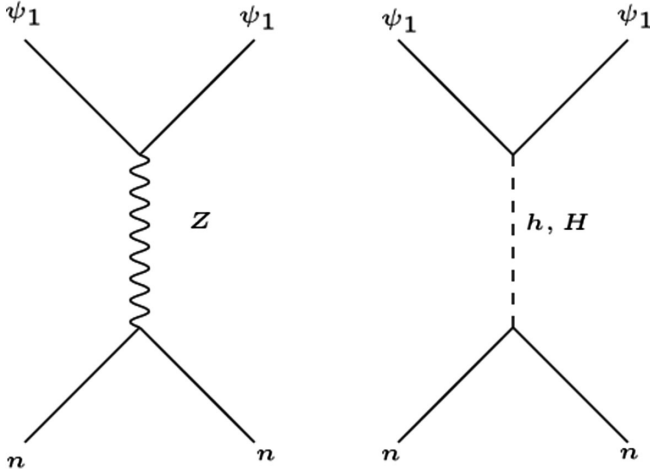


FIG. 5. Feynman graph showing DM-nucleon scattering via SM  $Z$  (left) and SM-like Higgs ( $h$ ) and heavier Higgs ( $H$ ) (right). Here  $n \in n, p$  stands for the nucleons.

$$\|\mathcal{M}\| = \sum_{i=1,2} [Zf_p^i + (A - Z)f_n^i]. \quad (33)$$

The effective couplings in Eq. (33) can be expressed as

$$f_{p,n}^i = \sum_{q=u,d,s} f_{T_q}^{p,n} \alpha_q^i \frac{m_{p,n}}{m_q} + \frac{2}{27} f_{T_G}^{p,n} \sum_{Q=c,t,b} \alpha_Q^i \frac{m_{p,n}}{m_Q}, \quad (34)$$

with

$$\alpha_q^1 = -\frac{\sqrt{2}Y \sin \theta \cos \theta \cos^2 \alpha m_q \cot \beta}{\sin \beta m_{h_1}^2 v_1}, \quad (35)$$

$$\alpha_q^2 = -\frac{\sqrt{2}Y \sin \theta \cos \theta \sin^2 \alpha m_q \cot \beta}{\sin \beta m_H^2 v_1}, \quad (36)$$

where  $f_T^{p,n}$  are nucleon form factors. For  $Z$ -mediated spin-independent direct detection, on the other hand, one can write the scattering cross section per nucleon as [40]

$$\sigma_{SI}^Z = \frac{1}{\pi A^2} \mu_r^2 \|\mathcal{M}\|^2, \quad (37)$$

with

$$\|\mathcal{M}\| = \sqrt{2}G_F \left[ Z \left( \frac{f_p}{f_n} + (A - Z) \right) \right] f_n \sin^2 \theta, \quad (38)$$

where  $f_{p,n}$  are again suitable nucleon form factors.<sup>3</sup> For simplicity, we can assume conservation of isospin, i.e.,  $f_p/f_n = 1$ . Here one should note that the  $Z$  mediation also gives rise to a spin-dependent direct search cross section.

<sup>3</sup>For the numerical values of all form factors, we have relied on the default assignments of the micROMEGAS package.

But the order of magnitude of such a spin-dependent cross section being extremely small compared to that of spin-independent ones, we choose to ignore that.<sup>4</sup>

In the top left panel in Fig. 6, we have illustrated the relic density allowed parameter space that survives the present spin-independent direct detection bound from XENON1T for  $\tan \beta = 1.3$ . We see a moderate range of  $\sin \theta$ 's are allowed by a direct search:  $0.01 \lesssim \sin \theta \lesssim 0.3$ . This is expected, as the direct detection cross section is proportional to  $\sin^2 \theta$  for scalar mediation and  $\sin^4 \theta$  for gauge mediation. As a consequence, smaller mixing should give rise to smaller  $\sigma_{SI}$ , making the DM parameter space more viable from the direct search bound. The presence of the second Higgs helps in keeping the VLF mixing within a moderate limit, unlike the case in Ref. [32], where the bound on the mixing is even more stringent due to the presence of only one (SM) Higgs. This is a consequence of the  $\frac{\sin^2 \alpha}{m_H^2}$  suppression due to the heavier Higgs and small scalar mixing in the case of scalar-mediated elastic scattering. This is also possible due to some cancellation between the Higgs-mediated diagrams leading to a destructive interference that allows one to choose  $\sin \theta$  as large as  $\sim 0.3$  without getting disallowed by the direct search exclusion. Also note here that most of the allowed parameter space lies just above the neutrino floor [128] and, hence, can still be probed by the future direct search experiments with improved sensitivity. In summary, constraints from the requirement of right relic abundance, together with the direct search exclusion limit, allows the VLF mixing to vary within a range of  $0.01 \lesssim \sin \theta \lesssim 0.3$  for a DM mass starting from around 100 GeV up to 3 TeV. The presence of the second Higgs helps the model to evade the present direct search bound and allows the parameter space to fit just above the neutrino floor, leaving the window open to either get discovered or get discarded from the very next limit on a spin-independent direct search. The top right panel in Fig. 6 shows the same with  $\tan \beta = 5$ .

In the bottom left panel in Fig. 6, we show the residual parameter space satisfying both relic abundance and direct detection bounds in the  $m_{\psi_1}$ - $\Delta m$  plane with respect to the variation of the VLF mixing  $\sin \theta$  for  $\tan \beta = 1.3$ . This clearly shows that  $\Delta m \lesssim 1.5$  TeV (for DM mass  $\sim 500$  GeV) in order to abide by both relic abundance and spin-independent direct detection bounds for  $\sin \theta \lesssim 0.3$ . For larger  $\tan \beta$ , shown in the right panel in Fig. 6, the bound on  $\Delta m$  is a bit more relaxed, which allows it to  $\sim 2.5$  TeV but for a larger DM mass. However, the VLF mixing is rather restricted and can be as large as  $\sin \theta \sim 0.1$ , which helps in suitably choosing the Yukawa  $Y$  via Eq. (17).

<sup>4</sup>To give an order of estimate, the set of data  $\{\sin \theta, \Delta m, m_{\psi_1}\} = \{0.07, 366, 647\}$ , which gives rise to a correct relic abundance for  $\tan \beta = 5$ , produces a spin-independent direct detection cross section of  $\sim \mathcal{O}(10^{-10})$  pb, compared to a spin-dependent direct search cross section of  $\sim \mathcal{O}(10^{-50})$  pb.

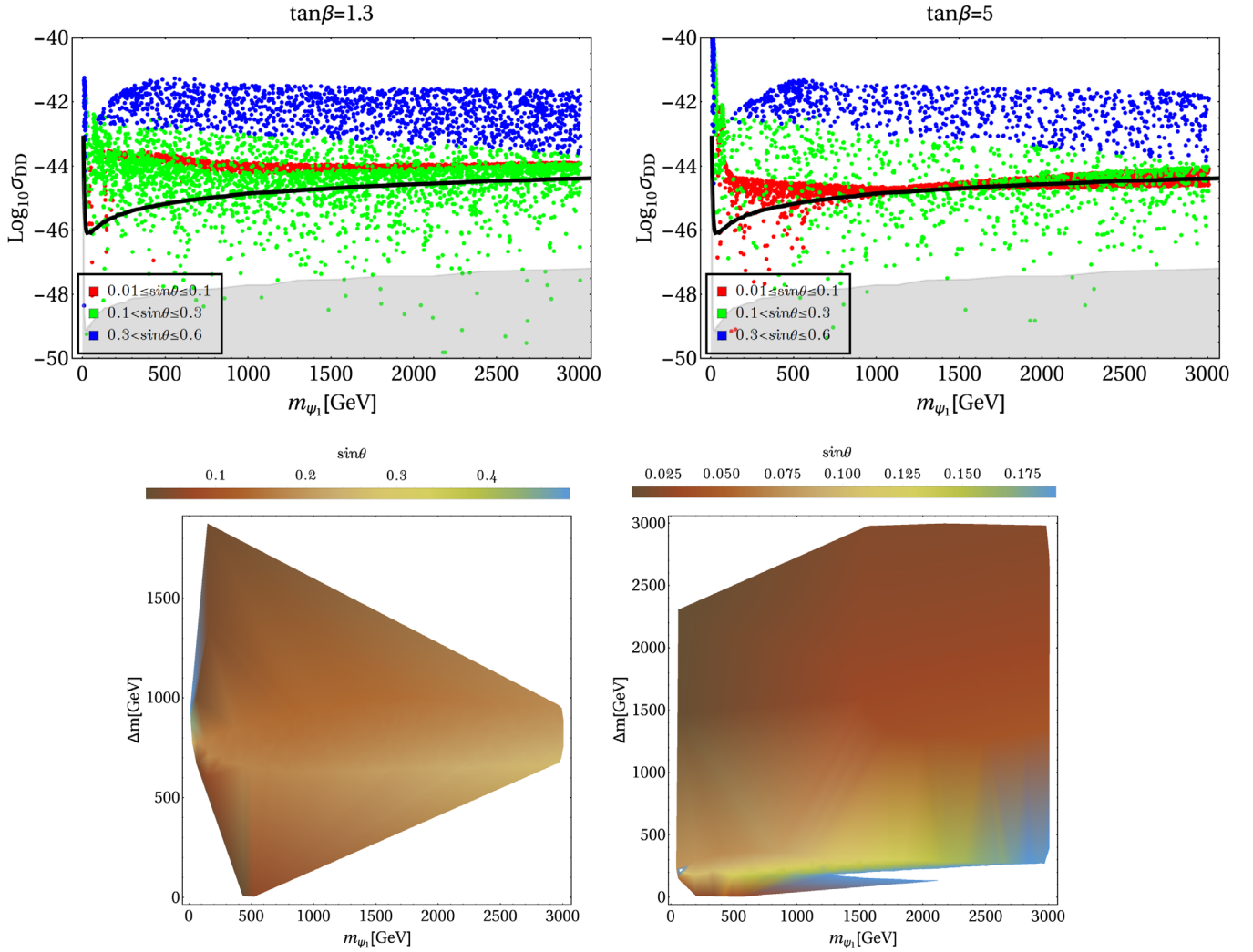


FIG. 6. Top left: Relic abundance allowed parameter space in the direct search plane for  $\tan\beta = 1.3$  for different choices of VLF mixing:  $0.01 \leq \sin\theta \leq 0.1$  in red,  $0.1 < \sin\theta \leq 0.3$  in green, and  $0.3 < \sin\theta \leq 0.6$  in blue, respectively, for  $\tan\beta = 1.3$ . Top right: The same as the top left with  $\tan\beta = 5$  (color codes remain unchanged). In both the plots, the thick black curve is the exclusion limit from the XENON1T experiment. Bottom left: Resulting parameter space satisfying both relic abundance and spin-independent direct detection for  $\tan\beta = 1.3$  in the  $m_{\psi_1}$ - $\Delta m$  plane, where the color bar shows different values of  $\sin\theta$ . Bottom right: The same as the bottom left with  $\tan\beta = 5$ .

The bound on  $\Delta m$  is crucial, as larger  $\Delta m$  results in larger missing energy, which, in turn, helps the model to be separated from the SM background at the colliders, as we shall explain in Sec. V. For smaller  $\Delta m$ , the model can

still be found at the colliders via a stable charged track signature.

Before moving on to the collider analysis, we have tabulated some of the benchmark points (BPs) in Table II.

TABLE II. Choices of the benchmark points for collider analysis. Masses, mixings, relic density, and direct search cross sections for the DM candidate are tabulated. In each case, the corresponding values of  $S$  and  $T$  parameters are also quoted.

Benchmark point	$\sin\theta$	$\Delta m$ (GeV)	$m_{\psi_1}$ (GeV)	$10^3 \hat{S}$	$10^3 \hat{T}$	$\tan\beta$	$m_{12}$ (GeV)	$\sigma_{DD}$ (cm <sup>2</sup> )	$\Omega h^2$
BP1	0.06	966	143	$4.06 \times 10^{-2}$	$2.94 \times 10^{-3}$	1.3	176	$6.14 \times 10^{-47}$	0.122
BP2	0.19	628	1175	$6.96 \times 10^{-1}$	$1.25 \times 10^{-2}$	1.3	185	$1.50 \times 10^{-45}$	0.119
BP3	0.05	383	60	$1.21 \times 10^{-2}$	$2.19 \times 10^{-4}$	1.3	176	$5.56 \times 10^{-47}$	0.121
BP4	0.08	369	804	$1.08 \times 10^{-1}$	$1.14 \times 10^{-4}$	5	125	$1.05 \times 10^{-45}$	0.121
BP5	0.22	218	72	$1.70 \times 10^{-1}$	$1.73 \times 10^{-2}$	5	130	$9.77 \times 10^{-48}$	0.121
BP6	0.03	10	256	$6.81 \times 10^{-3}$	$2.03 \times 10^{-11}$	5	125	$6.23 \times 10^{-47}$	0.121

TABLE III. Variation of the final state signal cross section with the MET cut for a fixed cut on  $H_T > 300$  GeV. All simulations are done at  $\sqrt{s} = 14$  TeV.

Benchmark points	$\sigma_{\psi^+\psi^-}$ (fb)	$\cancel{E}$ (GeV)	$H_T > 300$ GeV	$\sigma^{\text{OSD}}$ (fb)
BP1	$1.12 \times 10^{-1}$	>100	$H_T > 300$ GeV	$2.51 \times 10^{-2}$
		>200		$1.97 \times 10^{-2}$
		>300		$1.39 \times 10^{-2}$
BP2	$3.94 \times 10^{-3}$	>100	$H_T > 300$ GeV	$7.43 \times 10^{-4}$
		>200		$5.46 \times 10^{-4}$
		>300		$3.47 \times 10^{-4}$
BP3	9.95	>100	$H_T > 300$ GeV	$5.60 \times 10^{-1}$
		>200		$2.01 \times 10^{-1}$
		>300		$6.94 \times 10^{-2}$
BP4	$7.77 \times 10^{-2}$	>100	$H_T > 300$ GeV	$8.19 \times 10^{-3}$
		>200		$3.75 \times 10^{-3}$
		>300		$1.23 \times 10^{-3}$
BP5	52.26	>100	$H_T > 300$ GeV	$5.95 \times 10^{-1}$
		>200		$1.94 \times 10^{-1}$
		>300		$5.22 \times 10^{-2}$

These BPs satisfy bounds from relic abundance, direct detection, and also those arising from EWPO. The BPs are listed in the decreasing order of  $\Delta m$ , where BP6 has the minimum  $\Delta m$ . We have also kept the DM mass  $< 2$  TeV to have a sizable  $\psi^\pm$  production cross section. As we shall show in Sec. V, BP(1–5) can be distinguished at the LHC, as they produce huge missing energy due to large  $\Delta m$  that helps to separate them from the SM background. On the other hand, due to very small  $\Delta m$  (specifically, as  $\Delta m < m_W$ ), BP6 can produce only a displaced vertex at the collider or can be searched at the ILC via missing energy excess as shown in Refs. [36,37,41].

## V. COLLIDER PHENOMENOLOGY

The detailed study of the collider signature for vectorlike fermions can be found in Refs. [32,36,37,41]. As we have already seen, due to the presence of the second Higgs doublet, large  $\sin\theta$  can be achieved, satisfying both relic density and direct detection. As a result, one need not be confined in small  $\Delta m$ , and a large  $\Delta m$  is also viable. Such large  $\Delta m$ 's are favorable in order to distinguish this model at the collider from the SM background [41,42]. It is to be noted that the charged component of the  $SU(2)_L$  doublet VLF can be produced at the LHC via SM  $Z$  and photon mediation. The charged VLF can further decay via on-shell and/or off-shell  $W$  (depending on whether  $\Delta M \gtrsim 80$  GeV or  $\Delta m \lesssim 80$  GeV) to the following final states:

- (i) hadronically quiet opposite sign dilepton (OSD) with missing energy ( $\ell^+\ell^- + \cancel{E}$ ),
- (ii) single lepton, with two jets plus missing energy ( $\ell^\pm + jj + \cancel{E}$ ), and
- (iii) four jets plus missing energy ( $jjjj + \cancel{E}$ ).

We shall focus only on the leptonic final states (hadronically quiet dilepton), as they are much cleaner compared to

others. The Feynman graph for such a process is depicted in the lhs of Fig. 7. In the rhs of Fig. 7, we have shown the variation of the pair production cross section of the charged component of the VLF with a VLF mass at  $\sqrt{s} = 14$  TeV. As one can see, the production cross section decreases with an increase in the charged VLF mass showing the usual nature. We have also shown the position of different BPs on the same plot. As one can notice, BP6 has the highest production cross section, while BP2 has the least. This is evident from the fact that for BP6  $\Delta m = 10$  GeV, giving rise to a charged VLF mass of  $m_{\psi^\pm} = 276$  GeV. On the other hand BP2 has a larger  $\Delta m$  but the highest DM mass, which gives rise to  $m_{\psi^\pm} = 1803$  GeV, much larger than that for BP4.

### A. Object reconstruction and simulation details

As already mentioned, we implemented this model in LanHEP-3.3.2, and the parton level events are generated in CalcHEP-3.7.3 [129]. Those events are then fed to PYTHIA-6.4 [130] for showering and hadronization. The dominant SM backgrounds that can imitate our final state are generated in MADGRAPH-2.6.6 [131], and the corresponding production cross sections are multiplied with the appropriate  $K$  factor [132] in order to match with the next-to-leading-order cross sections. For all cases, we have used CTEQ6l as the parton distribution function [133]. Now, in order to mimic the collider environment, all the leptons, jets, and unclustered objects have been reconstructed assuming the following criteria:

- (i) *Lepton* ( $l = e, \mu$ ).—Leptons are identified with a minimum transverse momentum  $p_T > 20$  GeV and pseudorapidity  $|\eta| < 2.5$ . Two leptons can be distinguished as separate objects if their mutual distance in the  $\eta$ - $\phi$  plane is  $\Delta R = \sqrt{(\Delta\eta)^2 + (\Delta\phi)^2} \geq 0.2$ ,

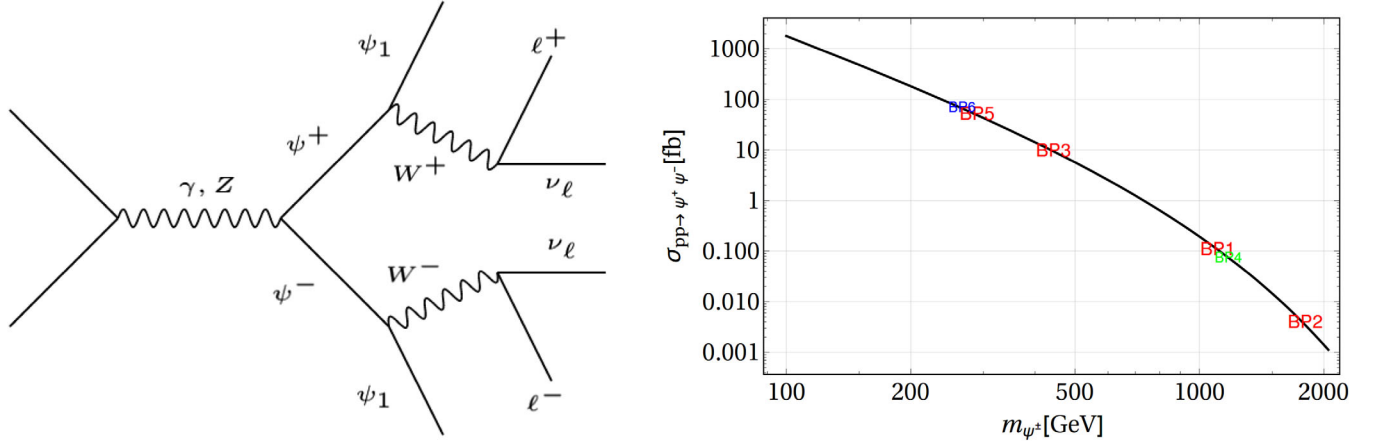


FIG. 7. Left: Pair production of charged VLFs and their subsequent decay to the OSD +  $\cancel{E}T$  final state. Right: Variation of the production cross section of  $\psi^\pm$  with  $m_{\psi^\pm}$  for  $\Delta m = 10$  GeV and center of mass energy  $\sqrt{s} = 14$  TeV. The production cross sections corresponding to different BPs are also shown in red, green, and blue on top of the curve.

while the separation between a lepton and a jet needs to be  $\Delta R \geq 0.4$ .

- (ii) *Jets ( $j$ ).*—All the partons within  $\Delta R = 0.4$  from the jet initiator cell are included to form the jets using the cone jet algorithm PYCELL built in PYTHIA. We demand  $p_T > 20$  GeV for a clustered object to be considered as a jet. Jets are isolated from unclustered objects if  $\Delta R > 0.4$ .
- (iii) *Unclustered objects.*—All the final state objects which are neither clustered to form jets nor identified as leptons belong to this category. Particles with  $0.5 < p_T < 20$  GeV and  $|\eta| < 5$  are considered as unclustered. Although unclustered objects do not intervene with our signal definition, they are important in constructing the missing energy of the events.
- (iv) *Missing energy ( $\cancel{E}_T$ ).*—The transverse momentum of all the missing particles (those are not registered in the detector) can be estimated from the momentum imbalance in the transverse direction associated to the visible particles. Missing energy (MET) is thus defined as

$$\cancel{E}_T = -\sqrt{\left(\sum_{\ell,j} p_x\right)^2 + \left(\sum_{\ell,j} p_y\right)^2}, \quad (39)$$

where the sum runs over all visible objects that include the leptons, jets, and unclustered components.

- (v) *Invariant dilepton mass ( $m_{\ell\ell}$ ).*—We can construct the invariant dilepton mass variable for two opposite sign leptons by defining

$$m_{\ell\ell}^2 = (p_{\ell^+} + p_{\ell^-})^2. \quad (40)$$

The invariant mass of OSD events, if created from a single parent, peaks at the parent mass, for example,

the Z boson. As the signal events (Fig. 7) do not arise from a single parent particle, the invariant mass cut plays a key role in eliminating the Z-mediated SM background.

- (vi)  *$H_T$ .*— $H_T$  is defined as the scalar sum of all isolated jets and lepton  $p_T$ 's:

$$H_T = \sum_{\ell,j} p_T. \quad (41)$$

For our signal, the sum includes only the two leptons that are present in the final state.

We shall use different cuts on these observables depending on their distribution patterns to separate the signal from the SM backgrounds. Thus, we can predict the significance as a function of the integrated luminosity. These are discussed in the following sections.

## B. Event rates and signal significance

In Fig. 8, we have shown the distribution of a normalized number of events with respect to MET (lhs) and  $H_T$  (rhs) for all the chosen BPs. In the same plot, we have also shown the distribution from dominant SM backgrounds that can mimic our signal. For the SM, the only source of MET are the SM neutrinos, which are almost massless with respect to the center of mass energy of the collider. As a result, the MET and  $H_T$  distribution for SM peaks up at a lower value, while for the model on top of the SM neutrinos MET arises from the DM  $\psi_1$  which is massive, and, hence, the corresponding distributions for the signals are much flattened. The notable feature in these plots is the fact that for larger  $\Delta m$  the signal distributions are well separated from that of the background. This is due to the fact that the peak of the MET distribution is determined by how much of  $p_T$  is being carried away by the missing particle

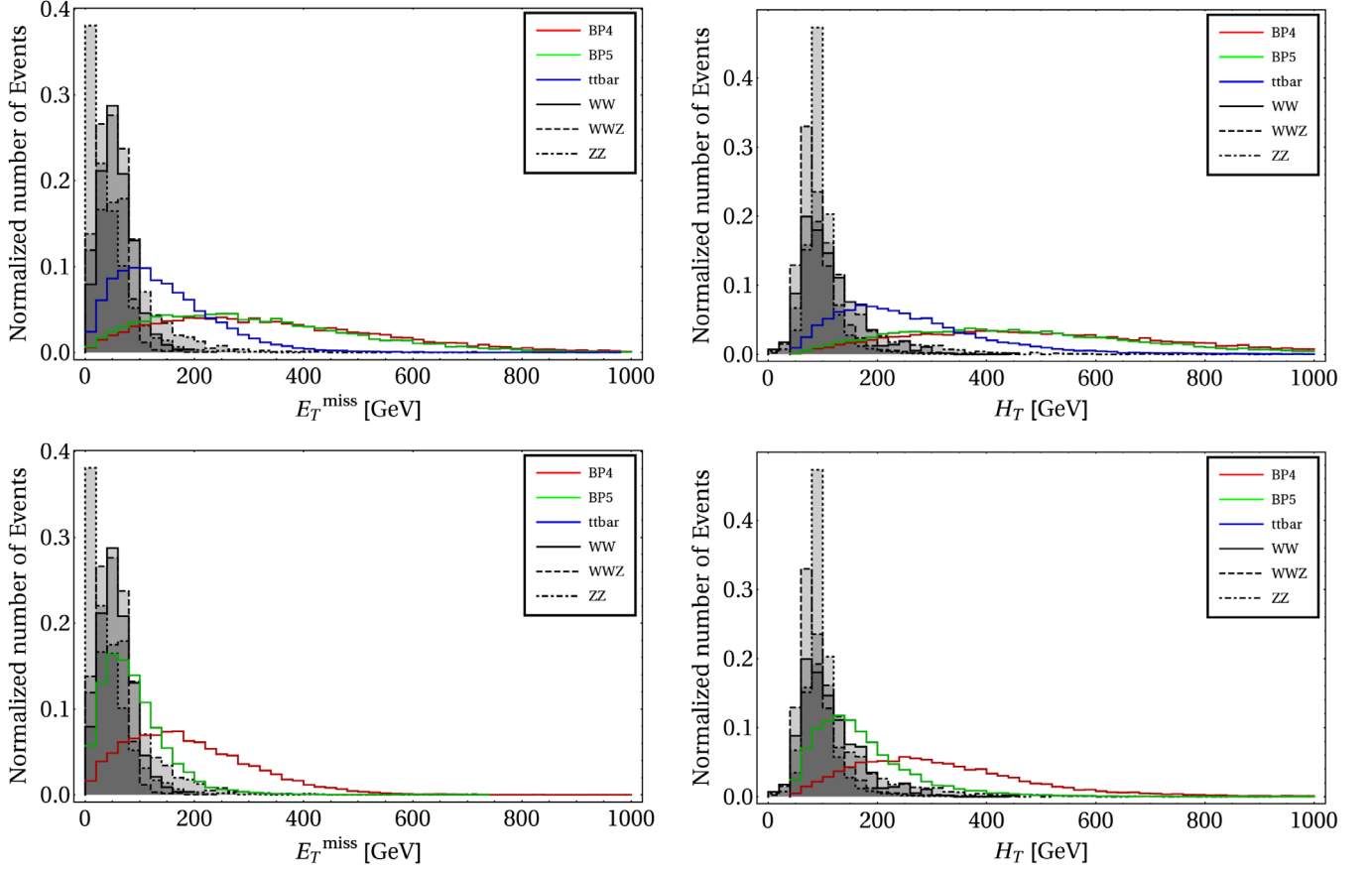


FIG. 8. Top left: Distribution of the normalized number of signal and background events with MET for BP(1,2,3). Top right: Distribution of normalized number of events with  $H_T$  for BP(1,2,3). Bottom left: The same as the top left but for BP(4,5). Bottom right: The same as the top right but for BP(4,5). In all cases, the black and gray histograms correspond to the dominant SM backgrounds. All simulations are done at  $\sqrt{s} = 14$  TeV with CTEQ61 as the parton distribution function. Note that we do not show the corresponding distributions for BP6, since due to very small  $\Delta m$  it is indistinguishable from the SM backgrounds.

(i.e., the DM), which, in turn, depends on the mass difference of the charged and neutral component of the VLF, i.e.,  $\Delta m$ . Hence, for larger  $\Delta m$  the DM carries away most of the  $p_T$ , making the distribution much flatter, while for smaller  $\Delta m$  the distribution peaks up at a lower value, as the produced DM particles are not boosted enough. As a consequence, BP1 and BP2 have the most flattened distribution, while BP(3,4,5) are increasingly overwhelmed by the SM background. Since BP6 has the smallest  $\Delta m$ , we refrain from showing this in the plots, as BP6 will be inseparable from the SM backgrounds. From these distributions, it is quite evident that with a cut on MET  $\gtrsim 200$  GeV and on  $H_T \gtrsim 300$  GeV (Table III) one can get rid of the SM backgrounds, retaining most of the signals. This is also reflected in Tables II and IV, where we have tabulated the cross section corresponding to final state OSD +  $\cancel{E}T$  events for the BPs and for the SM backgrounds, respectively. In order to understand the effectiveness of the choice of our cuts, we have shown the cut flow for an increasing choice of  $\cancel{E}$ , keeping the  $H_T$  fixed. Note that, for the signal (Table II), the final state cross section in

each case gradually diminishes with an increase in the MET cut; i.e., the harder the cut, the lesser is the cross section. The same is also true for the SM backgrounds as shown in Table IV. Note that, for the backgrounds, the

TABLE IV. Variation of the final state SM background cross section with the MET cut for a fixed cut on  $H_T > 250$  GeV. All simulations are done at  $\sqrt{s} = 14$  TeV.

Processes	$\sigma_{\text{production}}$ (pb)	$\cancel{E}$ (GeV)	$H_T > 300$ GeV	$\sigma^{\text{OSD}}$ (fb)
$t\bar{t}$	814.64	>100	$H_T > 300$ GeV	0
		>200		0
		>300		0
$W^+W^-$	99.98	>100		2.99
		>200		1.49
		>300		0
$W^+W^-Z$	0.15	>100		0.039
		>200		0.024
		>300		0.012
ZZ	14.01	>100		0
		>200		0
		>300		0

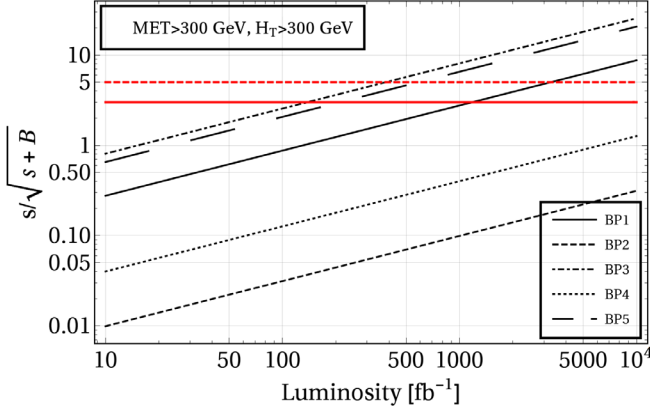


FIG. 9. Significance plotted against the integrated luminosity for the three benchmarks in Table II. The solid, dotted, and dot-dashed black lines correspond to different benchmark points. The solid red and dashed red lines denote  $3\sigma$  and  $5\sigma$  confidence, respectively.

most dominant one, i.e.,  $t\bar{t}$ , is completely killed by the zero jet veto. Among the rest,  $WW$  and  $WWZ$  still exist for  $\cancel{E} > 200$  GeV but can still be put to zero by a harder MET cut.  $ZZ$ , on the other hand, is again completely eliminated thanks to the invariant mass cut over a window of  $|m_Z \pm 50|$  GeV around the central value of  $Z$  mass. Thus, a wise choice of the cuts on the observables can help to completely get rid of the SM backgrounds while retaining most of the signal.

This can be translated into the signal significance for this model, which is shown in Fig. 9. Here we have plotted the significance of the chosen BPs with respect to the integrated luminosity. In order to minimize the SM background, we have employed  $\cancel{E} > 300$  GeV and  $H_T > 300$  GeV to compute the significance. We see, of all the BPs, BP(2,4) have the least possibility to be probed even with a luminosity as high as  $3000 \text{ fb}^{-1}$ . A large  $\Delta m$  in one way helps to distinguish BP(2,4) from the SM background, but due to the very small cross section at the production level the final state cross section becomes even smaller. This makes BP(2,4) least significant. For BP (1,3,5), on the other hand,  $\Delta m$  is optimum such that they can be separated from the background because of their larger missing energy, and at the same time the cross section is large enough so that a  $5\sigma$  significance can be achieved. Thus, we see BP3 and BP5 reach a discovery limit at a lower luminosity  $\sim 500 \text{ fb}^{-1}$ , while BP1 needs  $\sim 1000 \text{ fb}^{-1}$  for a  $5\sigma$  reach. Finally, we would like to mention that for all benchmarks with  $\Delta m \lesssim m_W$  (e.g., BP6) one can find a stable charged track due to the off-shell decay of the heavy charged VLF  $\psi^\pm$  via a  $W$  boson or they can also be probed at the ILC with a lower cut on MET. These scenarios have already been thoroughly investigated in Refs. [36,41]; hence, we do not discuss them here further.

## VI. STRONG FIRST-ORDER ELECTROWEAK PHASE TRANSITION AND GRAVITATIONAL WAVE SIGNALS

In this section, we would like to show the possibility of generation of stochastic GW from a SFOPT. The frequency of such GWs is well within the reach of the proposed GW detectors. The occurrence of a SFOPT and subsequent GW generation in context with the 2HDM has already been thoroughly studied [64,65]. In the context of our present model, we explore how such a detectable GW signal can be an alternate search strategy for singlet-doublet DM. The dynamics of the SFOPT is completely determined by the parameters of the scalar potential, as we shall see in the following sections. It is interesting to note that the choice of the scalar potential parameters agrees well with both the DM phenomenology and the GW generation, thus giving us a handle to probe the dark sector beyond DM and collider search experiments.

### A. Finite temperature effective potential

In order to explore the EWPT in the 2HDM, we need to include temperature corrections with the tree-level potential. In general, the finite temperature effective potential at temperature  $T$  can be expressed as [134]

$$V_{\text{eff}} = V_{\text{tree}} + V_{1\text{-loop}}^{T=0} + V_{1\text{-loop}}^{T \neq 0}, \quad (42)$$

where  $V_{\text{tree}}$ ,  $V_{1\text{-loop}}^{T=0}$ , and  $V_{1\text{-loop}}^{T \neq 0}$  are the tree-level potential at zero temperature, the Coleman-Weinberg one-loop effective potential at zero temperature, and the one-loop effective potential at a finite temperature, respectively. The tree-level potential  $V_{\text{tree}}$  can be obtained from Eq. (5) by replacing the fields  $\Phi_1$  and  $\Phi_2$  with their classical fields  $v_1$  and  $v_2$ , which is given by

$$V_{\text{tree}} = \frac{1}{2} m_{11}^2 v_1^2 + \frac{1}{2} m_{22}^2 v_2^2 - \frac{1}{2} m_{12}^2 v_1 v_2 + \frac{1}{8} \lambda_1 v_1^4 + \frac{1}{8} \lambda_2 v_2^4 + \frac{1}{4} (\lambda_3 + \lambda_4 + \lambda_5) v_1^2 v_2^2. \quad (43)$$

The Coleman-Weinberg one-loop effective potential at zero temperature  $V_{1\text{-loop}}^{T=0}$  can be written as [134,135]

$$V_{1\text{-loop}}^{T=0} = \pm \frac{1}{64\pi^2} \sum_i n_i m_i^4 \left[ \log \frac{m_i^2}{Q^2} - C_i \right], \quad (44)$$

where the  $+$  sign corresponds to bosons and the  $-$  sign corresponds to fermions. The sum  $i$  is over the Goldstone bosons  $G^\pm$ ,  $G$ ,  $A$ , and  $H^\pm$ , Higgs bosons  $h$  and  $H$ , gauge bosons  $W^\pm$  and  $Z$ , and the top fermion  $t$ . The field-dependent squared masses  $m_i^2$  for the top quark and gauge bosons at  $T = 0$  are given by

$$m_t^2 = \frac{1}{2} y_t^2 v_2^2 / s_\beta^2, \quad (45)$$

$$m_W^2 = \frac{1}{4}g^2(v_1^2 + v_2^2), \quad (46)$$

$$m_Z^2 = \frac{1}{4}(g^2 + g'^2)(v_1^2 + v_2^2), \quad (47)$$

where  $y_t$ ,  $g$ , and  $g'$  are the top Yukawa coupling and  $SU(2)_L$  and  $U(1)_Y$  gauge couplings of the SM, respectively.

The field-dependent squared masses  $m_i^2$  at  $T = 0$  for the scalar bosons can be obtained by diagonalizing the following matrices:

$$m_{h,H}^2 = \begin{pmatrix} m_{11}^2 + \frac{3}{2}\lambda_1 v_1^2 + \frac{1}{2}(\lambda_3 + \lambda_4 + \lambda_5)v_2^2 & -\frac{1}{2}m_{12}^2 + (\lambda_3 + \lambda_4 + \lambda_5)v_1 v_2 \\ -\frac{1}{2}m_{12}^2 + (\lambda_3 + \lambda_4 + \lambda_5)v_1 v_2 & m_{22}^2 + \frac{3}{2}\lambda_2 v_2^2 + \frac{1}{2}(\lambda_3 + \lambda_4 + \lambda_5)v_1^2 \end{pmatrix}, \quad (48)$$

$$m_{G,A}^2 = \begin{pmatrix} m_{11}^2 + \frac{1}{2}\lambda_1 v_1^2 + \frac{1}{2}\lambda_3 v_2^2 & -\frac{1}{2}m_{12}^2 + \frac{1}{2}(\lambda_4 + \lambda_5)v_1 v_2 \\ -\frac{1}{2}m_{12}^2 + \frac{1}{2}(\lambda_4 + \lambda_5)v_1 v_2 & m_{22}^2 + \frac{1}{2}\lambda_2 v_2^2 + \frac{1}{2}\lambda_3 v_1^2 \end{pmatrix}, \quad (49)$$

$$m_{G^\pm, H^\pm}^2 = \begin{pmatrix} 2m_{11}^2 + \lambda_1 v_1^2 + \lambda_3 v_2^2 & -m_{12}^2 + (\lambda_4 + \lambda_5)v_1 v_2 \\ -m_{12}^2 + (\lambda_4 + \lambda_5)v_1 v_2 & 2m_{22}^2 + \lambda_2 v_2^2 + \lambda_3 v_1^2 \end{pmatrix}. \quad (50)$$

Here we have applied the Landau gauge, where the Goldstones are massless at zero temperature ( $T = 0$ ) but at a finite temperature ( $T \neq 0$ ) they acquire a mass [59]. In Eq. (44),  $C_i$ 's are the renormalization-scheme-dependent numerical constant,  $Q$  is a renormalizable scale, and  $n_i$ 's are the number of degrees of freedom (DOF). For the gauge bosons ( $W, Z$ )  $C_{W,Z} = 5/6$ , and for the other particle species  $C_{h,H,G,A,H^+,H^-,G^+,G^-} = 3/2$  with the corresponding DOFs:  $n_{W^\pm} = 6$ ,  $n_Z = 3$ ,  $n_{h,H,G,A,H^+,H^-,G^+,G^-} = 1$ , and  $n_t = 12$ . The one-loop finite temperature effective potential  $V_{1\text{-loop}}^{T \neq 0}$  [Eq. (44)] reads [134]

$$V_{1\text{-loop}}^{T \neq 0} = \frac{T^2}{2\pi^2} \sum_i n_i J_\pm \left[ \frac{m_i^2}{T^2} \right], \quad (51)$$

where the functions  $J_\pm$  are

$$J_\pm \left( \frac{m_i^2}{T^2} \right) = \pm \int_0^\infty dy y^2 \log \left( 1 \mp e^{-\sqrt{y^2 + (m_i^2/T^2)}} \right). \quad (52)$$

In the finite temperature effective potential  $V_{1\text{-loop}}^{T \neq 0}$ , we include the temperature-corrected terms to the boson masses by following the Daisy resummation method [136]. In the Daisy resummation method, the thermal masses are [137–140]  $\mu_1^2(T) = m_{11}^2 + c_1 T^2$  and  $\mu_2^2(T) = m_{22}^2 + c_2 T^2$ , where

$$c_1 = \frac{3\lambda_1 + 2\lambda_3 + \lambda_4}{12} + \frac{3g^2 + g'^2}{16} + \frac{y_t^2}{4}, \quad (53)$$

$$c_2 = \frac{3\lambda_2 + 2\lambda_3 + \lambda_4}{12} + \frac{3g^2 + g'^2}{16}. \quad (54)$$

## B. Gravitational wave from SFOPT

The central idea of a FOPT is the bubble nucleation of a true vacuum state (from several metastable states) at a temperature commonly known as the nucleation temperature. The bubbles produced in this process can be of different sizes: small and large. The smaller bubbles tend to collapse, whereas the larger bubbles tend to expand after attaining the criticality. These bubbles of critical size then collide with each other, and their spherical symmetry is thus broken. This initiates the phase transition and subsequent production of the GW. The bubble nucleation rate per unit volume at a temperature  $T$  can be expressed as [141]

$$\Gamma = \Gamma_0(T) e^{-S_3(T)/T}, \quad (55)$$

where  $\Gamma_0(T) \propto T^4$  and  $S_3(T)$  denotes the Euclidean action of the critical bubble [141]:

$$S_3 = 4\pi \int dr r^2 \left[ \frac{1}{2}(\partial_t \vec{\phi})^2 + V_{\text{eff}} \right], \quad (56)$$

where  $V_{\text{eff}}$  is the effective finite temperature potential [Eq. (42)]. Bubble nucleation occurs at the nucleation temperature  $T_n$ , which satisfies the condition  $S_3(T_n)/T_n \approx 140$  [134].

As mentioned in Sec. I, GWs are produced from the FOPT mainly via three mechanisms, namely, bubble collisions [66–72], sound waves [73–76], and turbulence in the plasma [77–81]. The total GW intensity  $\Omega_{\text{GW}} h^2$  as a function of the frequency can be expressed as the sum of the contributions from the individual components [66–81]:

$$\Omega_{\text{GW}} h^2 = \Omega_{\text{col}} h^2 + \Omega_{\text{SW}} h^2 + \Omega_{\text{turb}} h^2. \quad (57)$$

The component from the bubbles collision  $\Omega_{\text{col}} h^2$  is given by (for an analytic and more accurate derivation, see [142,143])



$$\Omega_{\text{col}} h^2 = 1.67 \times 10^{-5} \left( \frac{\beta'}{H} \right)^{-2} \frac{0.11 v_w^3}{0.42 + v_w^2} \left( \frac{\kappa \alpha'}{1 + \alpha'} \right)^2 \times \left( \frac{g_*}{100} \right)^{-1/3} \frac{3.8 \left( \frac{f}{f_{\text{col}}} \right)^{2.8}}{1 + 2.8 \left( \frac{f}{f_{\text{col}}} \right)^{3.8}}, \quad (58)$$

where the parameter

$$\beta' = \left[ HT \frac{d}{dT} \left( \frac{S_3}{T} \right) \right] \Big|_{T_n}, \quad (59)$$

where  $T_n$  is the nucleation temperature and  $H_n$  is the Hubble parameter at  $T_n$ . The most general expression of the bubble wall velocity  $v_w$  can be written as<sup>5</sup> [71,145]

$$v_w = \frac{1/\sqrt{3} + \sqrt{\alpha'^2 + 2\alpha'/3}}{1 + \alpha'}. \quad (60)$$

The parameter  $\kappa$  in Eq. (58) is the fraction of latent heat deposited in a thin shell, which can be expressed as

$$\kappa = 1 - \frac{\alpha'_\infty}{\alpha'}, \quad (61)$$

with [85,92]

$$\alpha'_\infty = \frac{30}{24\pi^2 g_*} \left( \frac{v_n}{T_n} \right)^2 \left[ 6 \left( \frac{m_W}{v} \right)^2 + 3 \left( \frac{m_Z}{v} \right)^2 + 6 \left( \frac{m_t}{v} \right)^2 \right], \quad (62)$$

where  $v_n$  represents the vacuum expectation value of Higgs at  $T_n$  and  $m_W$ ,  $m_Z$ , and  $m_t$  are the masses of  $W$ ,  $Z$ , and top quarks, respectively. The parameter  $\alpha'$ , which is defined as the ratio of vacuum energy density  $\rho_{\text{vac}}$  released by the electroweak phase transition to the background energy density of the plasma  $\rho_*^{\text{rad}}$  at  $T_n$ , has the form

$$\alpha' = \left[ \frac{\rho_{\text{vac}}}{\rho_*^{\text{rad}}} \right] \Big|_{T_n} \quad (63)$$

with

$$\rho_{\text{vac}} = \left[ \left( V_{\text{eff}}^{\text{high}} - T \frac{dV_{\text{eff}}^{\text{high}}}{dT} \right) - \left( V_{\text{eff}}^{\text{low}} - T \frac{dV_{\text{eff}}^{\text{low}}}{dT} \right) \right] \quad (64)$$

and

$$\rho_{\text{rad}}^* = \frac{g_* \pi^2 T_n^4}{30}. \quad (65)$$

The quantity  $f_{\text{col}}$  in Eq. (58) is the peak frequency produced by the bubble collisions and reads

$$f_{\text{col}} = 16.5 \times 10^{-6} \text{ Hz} \left( \frac{0.62}{v_w^2 - 0.1 v_w + 1.8} \right) \times \left( \frac{\beta'}{H} \right) \left( \frac{T_n}{100 \text{ GeV}} \right) \left( \frac{g_*}{100} \right)^{1/6}. \quad (66)$$

The sound wave (SW) component of the gravitational wave [Eq. (57)] is given by

$$\Omega_{\text{SW}} h^2 = 2.65 \times 10^{-6} \left( \frac{\beta'}{H} \right)^{-1} v_w \left( \frac{\kappa_v \alpha'}{1 + \alpha'} \right)^2 \left( \frac{g_*}{100} \right)^{-1/3} \times \left( \frac{f}{f_{\text{SW}}} \right)^3 \left[ \frac{7}{4 + 3 \left( \frac{f}{f_{\text{SW}}} \right)^2} \right]^{7/2}, \quad (67)$$

where  $\kappa_v$  is the fraction of latent heat transformed into the bulk motion of the fluid, which can be expressed as

$$\kappa_v = \frac{\alpha'_\infty}{\alpha'} \left[ \frac{\alpha'_\infty}{0.73 + 0.083 \sqrt{\alpha'_\infty + \alpha'_\infty}} \right]. \quad (68)$$

In Eq. (67),  $f_{\text{SW}}$  denotes the peak frequency produced by the sound wave mechanisms, which has the following form:

$$f_{\text{SW}} = 1.9 \times 10^{-5} \text{ Hz} \left( \frac{1}{v_w} \right) \left( \frac{\beta'}{H} \right) \left( \frac{T_n}{100 \text{ GeV}} \right) \left( \frac{g_*}{100} \right)^{1/6}. \quad (69)$$

To check the contribution of the sound wave component to the total GW intensity, we need to estimate the suppression factor  $HR_*/\bar{U}_f$ , where  $\bar{U}_f$  denotes the root-mean-square (rms) fluid velocity and  $R_*$  denotes the mean bubble separation [85,146,147]. If the calculated suppression factor  $HR_*/\bar{U}_f$  of a given model comes out to be  $> 1$ , then the sound wave lasts more than a Hubble time; otherwise, it is an overestimate to the GW signal.

Finally, the component from the turbulence in the plasma  $\Omega_{\text{turb}} h^2$  is given by

$$\Omega_{\text{turb}} h^2 = 3.35 \times 10^{-4} \left( \frac{\beta'}{H} \right)^{-1} v_w \left( \frac{\epsilon \kappa_v \alpha'}{1 + \alpha'} \right)^{3/2} \times \left( \frac{g_*}{100} \right)^{-1/3} \frac{\left( \frac{f}{f_{\text{turb}}} \right)^3 \left( 1 + \frac{f}{f_{\text{turb}}} \right)^{-11/3}}{\left( 1 + \frac{8\pi f}{h_*} \right)}, \quad (70)$$

where  $\epsilon = 0.1$  and  $f_{\text{turb}}$  denotes the peak frequency produced by the turbulence mechanism which takes the form

$$f_{\text{turb}} = 2.7 \times 10^{-5} \text{ Hz} \left( \frac{1}{v_w} \right) \left( \frac{\beta'}{H} \right) \left( \frac{T_n}{100 \text{ GeV}} \right) \left( \frac{g_*}{100} \right)^{1/6}. \quad (71)$$

<sup>5</sup>A more detailed discussion on the choice of  $v_w$  can be found in Ref. [144].

TABLE V. Choice of the BPs allowed by DM phenomenology to investigate the phase transition properties and production of GWs.

BP	$m_{11}^2$ in GeV <sup>2</sup>	$m_{22}^2$ in GeV <sup>2</sup>	$m_{12}$ in GeV	$\lambda_1$	$\lambda_2$	$\lambda_3$	$\lambda_4$	$\lambda_5$	$\tan\beta$
I	27511.8	18531.5	176	6.05	2.00	6.63	-8.27	-8.27	1.3
II	36668.7	18503.2	185	0.79	0.45	11.54	-5.80	-5.80	1.3
III	70301.2	-4698.75	125	3.87	0.26	11.37	-5.63	-5.63	5
IV	76676.2	-4443.75	130	1.13	0.26	11.26	-5.52	-5.52	5

TABLE VI. Thermal parameters associated with the strong first-order electroweak phase transition (SFOEWPT) for the chosen four BPs.

BP	$T_c$ (GeV)	$\xi$	$v_n$ (GeV)	$T_n$ (GeV)	$\alpha'$	$\beta'/H$
I	71.36	1.71	125.73	66.86	0.26	3527
II	49.34	1.74	88.82	46.22	0.26	3571.17
III	62.39	1.17	75.87	61.33	0.12	14078.9
IV	58.88	1.21	73.74	57.79	0.13	13190.8

In Eq. (70), the parameter  $h_*$  can be written as

$$h_* = 16.5 \times 10^{-6} \text{ Hz} \left( \frac{T_n}{100 \text{ GeV}} \right) \left( \frac{g_*}{100} \right)^{1/6}. \quad (72)$$

Equations (57)–(72) are used for calculating the gravitational wave intensity. In order to study the phase transition properties and production of GWs in the present DM model, we choose four BPs (Table V) from the viable model parameter space. An EWPT takes place at the

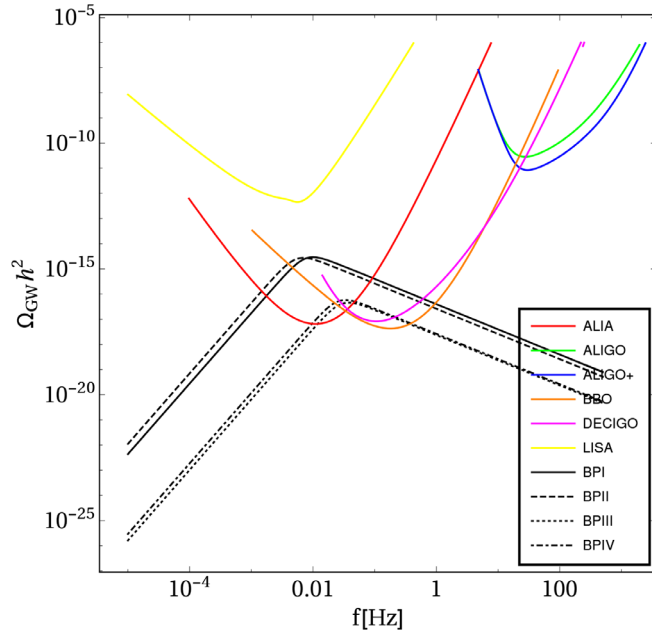


FIG. 10. Variation of GW intensity as a function of the frequency for the chosen four BPs with the sensitivity curves of ALIA, BBO, DECIGO, aLIGO, aLIGO+, and LISA detectors.

nucleation temperature, where a high phase and a low phase are separated by a potential barrier. The strength of the phase transition depends on the ratio of the VEVs  $v_c = \sqrt{\langle v_1 \rangle^2 + \langle v_2 \rangle^2}$ , measured at the critical temperature, to the critical temperature  $T_c$  at which two degenerate minima exist. If the condition  $\xi = v_c/T_c > 1$  is satisfied, then the SFOPT is said to have occurred [64].

The BPs in Table V are chosen in such a way that they not only satisfy constraints from the DM sector, but obey the condition for SFOPT as well. Thus, one should note here that the choices of  $m_{12}$  and  $\tan\beta$  in Table V are in accordance with those in Table II. In Table VI, we present our calculated  $\xi$  value corresponding to the benchmarks in Table V. In Table VI, we also tabulate other thermal parameters:  $\{v_n, T_c, T_n, \alpha', \beta'/H\}$  for each of the BPs, which are further used for the calculation of GW intensity. From Table VI, one can see that the nucleation temperature  $T_n$  is smaller than the critical temperature  $T_c$  for each of the BPs. The renormalizable scale  $Q = 246.22$  GeV is fixed for the calculation.

We calculate the GW intensity using Eqs. (57)–(72). For computing the intensity, we need to first estimate the thermal parameters related to FOPT. In order to find them, we have used the Cosmotransition package [134]. The tree-level potential [Eq. (43)] is given as an input to this package, and the resulting thermal parameters are tabulated in Table VI. The GW intensity mainly depends on several factors, e.g., nucleation temperature  $T_n$ , bubble wall velocity  $v_w$ , strength of the FOPT  $\alpha'$ , and the parameter  $\beta'$ . As mentioned in Sec. VI B, the sound wave contribution to the total GW intensity depends on the suppression factor  $HR_*/\bar{U}_f$  depending on whether it lasts more than a Hubble time or not. We estimate the suppression factor  $HR_*/\bar{U}_f$  following Refs. [85, 146, 147] and found it to be  $< 1$  for all the BPs. Because of this fact, following Refs. [85, 146, 147], we include the suppression factor  $HR_*/\bar{U}_f$  to the sound wave component of the GW intensity. In Fig. 10, we have plotted and compared the GW intensities for the chosen benchmarks (Table V) as a function of the frequency against the power-law-integrated sensitivity<sup>6</sup> curves for future GW detectors such as ALIA, BBO, DECIGO, aLIGO, aLIGO+, and LISA following Refs. [149, 150]. The frequencies at which the GW intensities acquire a

<sup>6</sup>For an alternative approach, see [148].

maximum value are  $10^{-2}$ ,  $7 \times 10^{-3}$ ,  $3.80 \times 10^{-2}$ , and  $3.40 \times 10^{-2}$  Hz for BPI, BPII, BPIII, and BPIV, respectively. As is evident from Fig. 10, the GW intensities for all the BPs (BPI–BPIV) lie within the sensitivity curves of ALIA, BBO, and DECIGO. The upshot is thus to note the fact that the benchmark values of  $m_{12}$  and  $\tan\beta$  for DM phenomenology agree well with those of a successful SFOPT leading to the production of a detectable GW signal.

## VII. CONCLUSIONS

In this paper, we have proposed a singlet-doublet fermionic DM model, where the lightest fermion (odd under an imposed discrete symmetry  $\mathcal{Z}'_2$ ), emerging as a singlet-doublet admixture of VLFs, can be a viable DM candidate ( $\psi_1$ ). We extend the model with a second Higgs doublet, where the second Higgs is odd under another discrete symmetry  $\mathcal{Z}_2$ . The imposition of two different discrete symmetries is necessary to prevent the occurrence of the FCNC at tree level, while allowing a strong first-order phase transition within a consistent DM framework. The DM in this case is a weakly interacting massive particle that undergoes freeze-out to yield the Planck observed relic abundance. This is achieved via annihilation of the DM with itself, also via its coannihilation with its massive component ( $\psi_2$ ) and with the charged component ( $\psi^\pm$ ). As the doublet carries a  $SU(2)_L$  charge, hence, on top of scalar mediation, the annihilation channels are also SM gauge mediated. The presence of the  $Z$ -mediated direct search puts a strong bound on the model parameter space allowing the VLF mixing  $\sin\theta \lesssim 0.3$  for both  $\tan\beta = 1.3$  and  $\tan\beta = 5$  for a DM mass up to  $\gtrsim 1$  TeV. The presence of the second Higgs makes the direct detection bounds less stringent. This is typically due to (a)  $\sin^2\alpha/m_H^2$  suppression from the heavier Higgs with small scalar mixing and (b) some destructive interference between the two scalar-mediated diagrams (the so-called blind spot) that offers some breathing space in the direct detection parameter space. Thus, one can still achieve a moderate  $\sin\theta$  in contrast with singlet-doublet models with only a SM Higgs. The model thus lives over a large parameter space, satisfying both relic abundance and spin-independent direct search bounds.

We have then explored possible signatures that this model can give rise to at the LHC. As the leptonic channels are cleaner, we have studied the hadronically quiet dilepton final states (HQ2L) where we see that a substantial signal significance is achievable (for an integrated luminosity  $\mathcal{L} \sim 300 \text{ fb}^{-1}$ ) by a judicious choice of cuts on the MET and  $H_T$ . This is again possible because of the presence of the second Higgs doublet that allows large  $\sin\theta$ , satisfying both relic abundance and direct search, which, in turn, allows a large  $\Delta m (\equiv m_{\psi^\pm} - m_{\psi_1}) \sim 1$  TeV. Larger  $\Delta m$  is the key to distinguish the signal from the dominant SM backgrounds exploiting hard cuts on MET and  $H_T$ . For

$\Delta m \lesssim m_W$  the model may be probed via a displaced vertex signature due to the off-shell decay of the charged VLF to SM leptons and neutrino.

We finally have looked into the possibility of getting a GW via a SFOPT due to the extended scalar sector. We have found that for both  $\tan\beta = \{1.3, 5\}$  the model is capable of producing a detectable GW signal modulo we tune the parameter  $m_{12}$  accordingly. The probability of getting a SFOPT is thus very sensitive to the choice of  $m_{12}$ . We see that, for some benchmark values of  $m_{12}$  and  $\tan\beta$ , one can have a detectable GW signal via SFOPT while satisfying all DM constraints. This model thus leaves us with the window of probing such singlet-doublet DM models via GW detectors even if other experiments give rise to null results.

## ACKNOWLEDGMENTS

B. B. and A. P. acknowledge the Workshop in High Energy Physics Phenomenology, IIT Guwahati, where a part of the work was completed. B. B. also acknowledges fruitful discussions with Eung Jin Chun. A. P. thanks Biswajit Banerjee for helping in modifying the Cosmotransition package. A. D. B. thanks Rishav Roshan for useful discussions. We thank Ryusuke Jinno for comments on GW analysis and providing useful references. The authors acknowledge A. Elbakyan for resources.

## APPENDIX: EXPRESSIONS FOR THE DECAY WIDTHS AND RELEVANT FEYNMANN DIAGRAMS

### 1. Invisible Higgs and $Z$ decay

The SM Higgs can decay to  $\psi_1$  pairs. Now, the combination of SM channels yields an observed (expected) upper limit on the Higgs branching fraction of 0.24 at 95% C.L. [151] with a total decay width  $\Gamma = 4.07 \times 10^{-3}$  GeV. On the other hand, the SM  $Z$  boson can also decay to DM pairs and, hence, constrained from observation:  $\Gamma_{\text{inv}}^Z = 499 \pm 1.5$  MeV [96]. So, if  $Z$  is allowed to decay into a  $\psi_1\psi_1$  pair, the decay width should not be more than 1.5 MeV.

TABLE VII. Invisible Higgs branching ratio and invisible  $Z$  decay width for different benchmark points tabulated in Tab. II. Only for BP3 the constraint from invisible Higgs branching ratio is applicable, which is  $\mathcal{O}(10^{-6})$  for  $\tan\beta = 1.3$  or  $\tan\beta = 5$ . Blank cells are “not applicable” for cases where  $m_{\psi_1} > m_Z(m_h)/2$ .

Benchmark point	$B_{\text{inv}}^{\text{higgs}}$	$\Gamma_{\text{inv}}^Z$ (MeV)
BP1		
BP2		
BP3	$\sim 10^{-6}$	
BP4		
BP5		
BP6		

Since either  $\Delta m$  [for BP(1,2,3,4,5,6)] or  $m_{\psi_1}$  is much larger than 100 GeV for all the benchmarks, neither  $Z$  nor  $h$  can decay to the heavier mass eigenstate  $\psi_2$ . Therefore, the expressions for  $H_1 \rightarrow \psi_1\psi_1$  and  $Z \rightarrow \psi_1\psi_1$  decay widths are given by

$$\Gamma_{\text{inv}}^{\text{higgs}}(H_1 \rightarrow \psi_1\psi_1) = \left( \frac{Y^2 \sin^2 \theta \cos^2 \theta \sin^2 \alpha}{8\pi} \right) m_{h_1} \left( 1 - \frac{4m_{\psi_1}^2}{m_{h_1}^2} \right)^{3/2}, \quad (\text{A1})$$

$$\Gamma_{\text{inv}}^Z(Z \rightarrow \psi_1\psi_1) = \frac{m_Z}{48\pi} \frac{e^2 \sin^4 \theta}{\sin^2 \theta_W \cos^2 \theta_W} \left( 1 + \frac{m_{\psi_1}^2}{m_Z^2} \right) \sqrt{1 - \frac{4m_{\psi_1}^2}{m_Z^2}}. \quad (\text{A2})$$

Note that for none of the benchmark points in Table II, except BP3, is either of the constraints from Higgs invisible decay branching or  $Z$ -boson invisible decay branching applicable. Since for BP3 the DM mass is 60 GeV, it is possible for the SM Higgs to decay to a pair of  $\psi_1$ . However, due to small VLF mixing, such a decay is well within the measured invisible decay rate of SM Higgs (Table VII).

## 2. Relevant Feynman diagrams for DM (co)annihilation

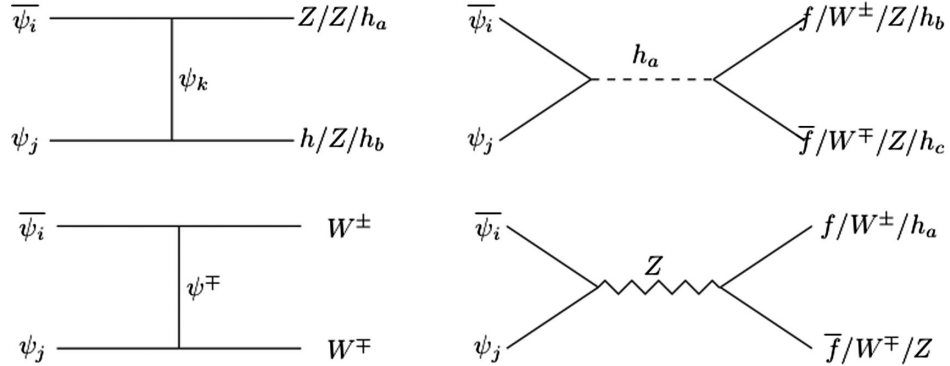


FIG. 11. Annihilation ( $i = j$ ) and coannihilation ( $i \neq j$ ) type number changing processes for vectorlike fermionic DM in the model. Here  $i, j, k = 1, 2$ ;  $a, b, c = 1, 2$ , and  $f$  stands for SM fermions.

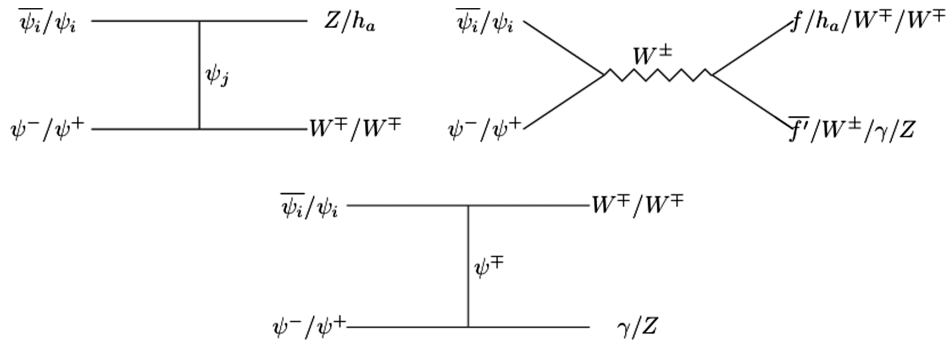


FIG. 12. Feynman diagrams for coannihilation type number changing processes of  $\psi_i$  ( $i = 1, 2$ ) with the charged component  $\psi^\pm$  to SM particles. Here  $f$  and  $f'$  stand for SM fermions ( $f \neq f'$ ).

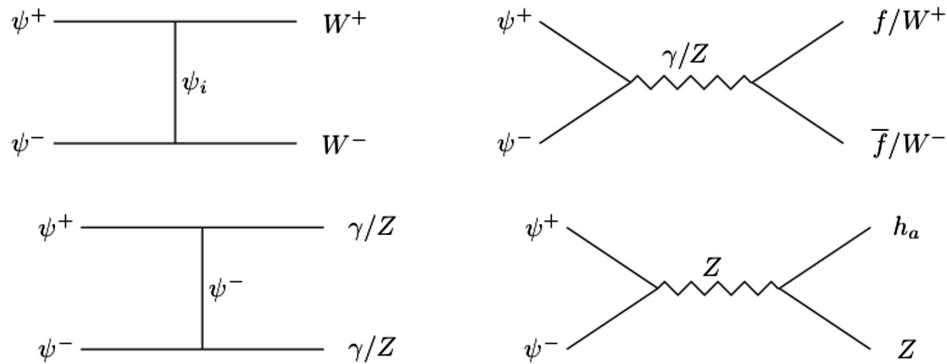


FIG. 13. Feynman diagrams for charged fermionic DM,  $\psi^\pm$  annihilation to SM particles in final states. Here  $a = 1, 2$ .

- [1] F. Zwicky, *Helv. Phys. Acta* **6**, 110 (1933) [*Gen. Relativ. Gravit.* **41**, 207 (2009)].
- [2] V. C. Rubin and W. K. Ford, Jr., *Astrophys. J.* **159**, 379 (1970).
- [3] D. Clowe, M. Bradac, A. H. Gonzalez, M. Markevitch, S. W. Randall, C. Jones, and D. Zaritsky, *Astrophys. J.* **648**, L109 (2006).
- [4] R. Massey, T. Kitching, and J. Richard, *Rep. Prog. Phys.* **73**, 086901 (2010).
- [5] N. Aghanim *et al.* (Planck Collaboration), [arXiv:1807.06209](https://arxiv.org/abs/1807.06209).
- [6] E. W. Kolb and M. S. Turner, *Front. Phys.* **69**, 1 (1990).
- [7] G. Arcadi, M. Dutra, P. Ghosh, M. Lindner, Y. Mambrini, M. Pierre, S. Profumo, and F. S. Queiroz, *Eur. Phys. J. C* **78**, 203 (2018).
- [8] D. S. Akerib *et al.* (LUX Collaboration), *Phys. Rev. Lett.* **118**, 251302 (2017).
- [9] A. Tan *et al.* (PandaX-II Collaboration), *Phys. Rev. Lett.* **117**, 121303 (2016).
- [10] X. Cui *et al.* (PandaX-II Collaboration), *Phys. Rev. Lett.* **119**, 181302 (2017).
- [11] E. Aprile *et al.* (XENON Collaboration), *J. Cosmol. Astropart. Phys.* **04** (2016) 027.
- [12] E. Aprile *et al.* (XENON Collaboration), *Phys. Rev. Lett.* **121**, 111302 (2018).
- [13] L. J. Hall, K. Jedamzik, J. March-Russell, and S. M. West, *J. High Energy Phys.* **03** (2010) 080.
- [14] Y. Hochberg, E. Kuflik, T. Volansky, and J. G. Wacker, *Phys. Rev. Lett.* **113**, 171301 (2014).
- [15] E. Kuflik, M. Perelstein, N. R.-L. Lorier, and Y.-D. Tsai, *J. High Energy Phys.* **08** (2017) 078.
- [16] H. Davoudiasl and G. Mohlabeng, [arXiv:1912.05572](https://arxiv.org/abs/1912.05572).
- [17] T. Lin, *Proc. Sci.*, 333 (2019) 009 [[arXiv:1904.07915](https://arxiv.org/abs/1904.07915)].
- [18] G. C. Branco, P. M. Ferreira, L. Lavoura, M. N. Rebelo, M. Sher, and J. P. Silva, *Phys. Rep.* **516**, 1 (2012).
- [19] W. Mader, J.-h. Park, G. M. Pruna, D. Stockinger, and A. Straessner, *J. High Energy Phys.* **09** (2012) 125; **01** (2014) 006.
- [20] C.-Y. Chen, in *Proceedings of the 2013 Community Summer Study on the Future of U.S. Particle Physics: Snowmass on the Mississippi (CSS2013): Minneapolis, MN, USA* (2013), <http://www.slac.stanford.edu/econf/C1307292/docs/submittedArxivFiles/1308.3487.pdf>.
- [21] G. Bhattacharyya and D. Das, *Pramana* **87**, 40 (2016).
- [22] P. Basler, P. M. Ferreira, M. Mühlleitner, and R. Santos, *Phys. Rev. D* **97**, 095024 (2018).
- [23] S. Gori, H. E. Haber, and E. Santos, *J. High Energy Phys.* **06** (2017) 110.
- [24] R. Mahbubani and L. Senatore, *Phys. Rev. D* **73**, 043510 (2006).
- [25] F. D'Eramo, *Phys. Rev. D* **76**, 083522 (2007).
- [26] R. Enberg, P. J. Fox, L. J. Hall, A. Y. Papaioannou, and M. Papucci, *J. High Energy Phys.* **11** (2007) 014.
- [27] T. Cohen, J. Kearney, A. Pierce, and D. Tucker-Smith, *Phys. Rev. D* **85**, 075003 (2012).
- [28] C. Cheung and D. Sanford, *J. Cosmol. Astropart. Phys.* **02** (2014) 011.
- [29] D. Restrepo, A. Rivera, M. Sánchez-Peláez, O. Zapata, and W. Tangarife, *Phys. Rev. D* **92**, 013005 (2015).
- [30] L. Calibbi, A. Mariotti, and P. Tziveloglou, *J. High Energy Phys.* **10** (2015) 116.
- [31] G. Cynolter, J. Kovács, and E. Lendvai, *Mod. Phys. Lett. A* **31**, 1650013 (2016).
- [32] S. Bhattacharya, N. Sahoo, and N. Sahu, *Phys. Rev. D* **93**, 115040 (2016).
- [33] A. Dutta Banik, D. Majumdar, and A. Biswas, *Eur. Phys. J. C* **76**, 346 (2016).
- [34] S. Bhattacharya, B. Karmakar, N. Sahu, and A. Sil, *J. High Energy Phys.* **05** (2017) 068.
- [35] S. Bhattacharya, B. Karmakar, N. Sahu, and A. Sil, *Phys. Rev. D* **93**, 115041 (2016).
- [36] S. Bhattacharya, N. Sahoo, and N. Sahu, *Phys. Rev. D* **96**, 035010 (2017).
- [37] S. Bhattacharya, P. Ghosh, N. Sahoo, and N. Sahu, *Front. Phys.* **7**, 80 (2019).
- [38] S. Bhattacharya, P. Ghosh, and N. Sahu, *J. High Energy Phys.* **02** (2019) 059.
- [39] A. Dutta Banik, A. K. Saha, and A. Sil, *Phys. Rev. D* **98**, 075013 (2018).
- [40] G. Arcadi, *Eur. Phys. J. C* **78**, 864 (2018).

- [41] B. Barman, S. Bhattacharya, P. Ghosh, S. Kadam, and N. Sahu, *Phys. Rev. D* **100**, 015027 (2019).
- [42] B. Barman, D. Borah, P. Ghosh, and A. K. Saha, *J. High Energy Phys.* **10** (2019) 275.
- [43] C. Cheung, L. J. Hall, D. Pinner, and J. T. Ruderman, *J. High Energy Phys.* **05** (2013) 100.
- [44] P. Huang and C. E. M. Wagner, *Phys. Rev. D* **90**, 015018 (2014).
- [45] A. Berlin, S. Gori, T. Lin, and L.-T. Wang, *Phys. Rev. D* **92**, 015005 (2015).
- [46] M. E. Cabrera, J. A. Casas, A. Delgado, and S. Robles, *arXiv:1912.01758*.
- [47] A. D. Sakharov, *Pis'ma Zh. Eksp. Teor. Fiz.* **5**, 32 (1967) [*Usp. Fiz. Nauk* **161**, 61 (1991)].
- [48] M. B. Gavela, P. Hernandez, J. Orloff, and O. Pene, *Mod. Phys. Lett. A* **09**, 795 (1994).
- [49] P. Huet and E. Sather, *Phys. Rev. D* **51**, 379 (1995).
- [50] M. B. Gavela, P. Hernandez, J. Orloff, O. Pene, and C. Quimbay, *Nucl. Phys.* **B430**, 382 (1994).
- [51] D. E. Morrissey and M. J. Ramsey-Musolf, *New J. Phys.* **14**, 125003 (2012).
- [52] H. Haber, G. Kane, and T. Sterling, *Nucl. Phys.* **B161**, 493 (1979).
- [53] L. J. Hall and M. B. Wise, *Nucl. Phys.* **B187**, 397 (1981).
- [54] J. F. Donoghue and L.-F. Li, *Phys. Rev. D* **19**, 945 (1979).
- [55] V. Barger, J. L. Hewett, and R. J. N. Phillips, *Phys. Rev. D* **41**, 3421 (1990).
- [56] M. Aoki, S. Kanemura, K. Tsumura, and K. Yagyu, *Phys. Rev. D* **80**, 015017 (2009).
- [57] G. C. Dorsch, S. J. Huber, and J. M. No, *J. High Energy Phys.* **10** (2013) 029.
- [58] G. C. Dorsch, S. J. Huber, K. Mimasu, and J. M. No, *Phys. Rev. Lett.* **113**, 211802 (2014).
- [59] P. Basler, M. Krause, M. Mühlleitner, J. Wittbrodt, and A. Wlotzka, *J. High Energy Phys.* **02** (2017) 121.
- [60] J. M. Cline and P.-A. Lemieux, *Phys. Rev. D* **55**, 3873 (1997).
- [61] L. Fromme, S. J. Huber, and M. Seniuch, *J. High Energy Phys.* **11** (2006) 038.
- [62] A. Haarr, A. Kvellestad, and T. C. Petersen, *arXiv:1611.05757*.
- [63] P. Basler, M. Mühlleitner, and J. Wittbrodt, *J. High Energy Phys.* **03** (2018) 061.
- [64] J. Bernon, L. Bian, and Y. Jiang, *J. High Energy Phys.* **05** (2018) 151.
- [65] X. Wang, F. P. Huang, and X. Zhang, *Phys. Rev. D* **101**, 015015 (2020).
- [66] A. Kosowsky, M. S. Turner, and R. Watkins, *Phys. Rev. D* **45**, 4514 (1992).
- [67] A. Paul, B. Banerjee, and D. Majumdar, *J. Cosmol. Astropart. Phys.* **10** (2019) 062.
- [68] A. Kosowsky and M. S. Turner, *Phys. Rev. D* **47**, 4372 (1993).
- [69] S. J. Huber and T. Konstandin, *J. Cosmol. Astropart. Phys.* **09** (2008) 022.
- [70] A. Kosowsky, M. S. Turner, and R. Watkins, *Phys. Rev. Lett.* **69**, 2026 (1992).
- [71] M. Kamionkowski, A. Kosowsky, and M. S. Turner, *Phys. Rev. D* **49**, 2837 (1994).
- [72] C. Caprini, R. Durrer, and G. Servant, *Phys. Rev. D* **77**, 124015 (2008).
- [73] M. Hindmarsh, S. J. Huber, K. Rummukainen, and D. J. Weir, *Phys. Rev. Lett.* **112**, 041301 (2014).
- [74] J. T. Giblin, Jr. and J. B. Mertens, *J. High Energy Phys.* **12** (2013) 042.
- [75] J. T. Giblin and J. B. Mertens, *Phys. Rev. D* **90**, 023532 (2014).
- [76] M. Hindmarsh, S. J. Huber, K. Rummukainen, and D. J. Weir, *Phys. Rev. D* **92**, 123009 (2015).
- [77] C. Caprini and R. Durrer, *Phys. Rev. D* **74**, 063521 (2006).
- [78] T. Kahnashvili, A. Kosowsky, G. Gogoberidze, and Y. Maravin, *Phys. Rev. D* **78**, 043003 (2008).
- [79] T. Kahnashvili, L. Campanelli, G. Gogoberidze, Y. Maravin, and B. Ratra, *Phys. Rev. D* **78**, 123006 (2008); **79**, 109901(E) (2009).
- [80] T. Kahnashvili, L. Kisslinger, and T. Stevens, *Phys. Rev. D* **81**, 023004 (2010).
- [81] C. Caprini, R. Durrer, and G. Servant, *J. Cosmol. Astropart. Phys.* **12** (2009) 024.
- [82] X. Gong *et al.*, *J. Phys. Conf. Ser.* **610**, 012011 (2015).
- [83] G. M. Harry, P. Fritschel, D. A. Shaddock, W. Folkner, and E. S. Phinney, *Classical Quantum Gravity* **23**, 4887 (2006); **23**, 7361(E) (2006).
- [84] N. Seto, S. Kawamura, and T. Nakamura, *Phys. Rev. Lett.* **87**, 221103 (2001).
- [85] C. Caprini *et al.*, *J. Cosmol. Astropart. Phys.* **04** (2016) 001.
- [86] Gregory M. Harry (LIGO Scientific Collaboration), *Classical Quantum Gravity* **27**, 084006 (2010).
- [87] P. Schwaller, *Phys. Rev. Lett.* **115**, 181101 (2015).
- [88] A. Beniwal, M. Lewicki, J. D. Wells, M. White, and A. G. Williams, *J. High Energy Phys.* **08** (2017) 108.
- [89] R.-G. Cai, Z. Cao, Z.-K. Guo, S.-J. Wang, and T. Yang, *Natl. Sci. Rev.* **4**, 687 (2017).
- [90] M. R. Buckley and A. H. G. Peter, *Phys. Rep.* **761**, 1 (2018).
- [91] A. Alves, T. Ghosh, H.-K. Guo, K. Sinha, and D. Vagie, *J. High Energy Phys.* **04** (2019) 052.
- [92] V. R. Shajee and A. Tofighi, *Eur. Phys. J. C* **79**, 360 (2019).
- [93] L. Bian and Y.-L. Tang, *J. High Energy Phys.* **12** (2018) 006.
- [94] A. Mohamadnejad, *arXiv:1907.08899*.
- [95] G. Bertone *et al.*, *arXiv:1907.10610*.
- [96] M. Tanabashi *et al.* (Particle Data Group), *Phys. Rev. D* **98**, 030001 (2018).
- [97] N. Chakrabarty and B. Mukhopadhyaya, *Eur. Phys. J. C* **77**, 153 (2017).
- [98] I. P. Ivanov, *Phys. Rev. D* **75**, 035001 (2007); **76**, 039902(E) (2007).
- [99] M. Maniatis, A. von Manteuffel, O. Nachtmann, and F. Nagel, *Eur. Phys. J. C* **48**, 805 (2006).
- [100] X.-J. Xu, *Phys. Rev. D* **95**, 115019 (2017).
- [101] A. Arhrib, in *Proceedings of the Workshop on Non-commutative Geometry, Superstrings and Particle Physics Rabat, Morocco* (2000), *arXiv:hep-ph/0012353*.
- [102] I. F. Ginzburg and I. P. Ivanov, *arXiv:hep-ph/0312374*.
- [103] I. F. Ginzburg and I. P. Ivanov, *Phys. Rev. D* **72**, 115010 (2005).

- [104] G. C. Dorsch, S. J. Huber, T. Konstandin, and J. M. No, *J. Cosmol. Astropart. Phys.* **05** (2017) 052.
- [105] H.-J. He, N. Polonsky, and S.-f. Su, *Phys. Rev. D* **64**, 053004 (2001).
- [106] W. Grimus, L. Lavoura, O. M. Ogreid, and P. Osland, *J. Phys. G* **35**, 075001 (2008).
- [107] W. Grimus, L. Lavoura, O. M. Ogreid, and P. Osland, *Nucl. Phys.* **B801**, 81 (2008).
- [108] G. Cynolter and E. Lendvai, *Eur. Phys. J. C* **58**, 463 (2008).
- [109] R. Barbieri, A. Pomarol, R. Rattazzi, and A. Strumia, *Nucl. Phys.* **B703**, 127 (2004).
- [110] G. Abbiendi *et al.* (ALEPH, DELPHI, L3, OPAL, and LEP Collaborations), *Eur. Phys. J. C* **73**, 2463 (2013).
- [111] A. Arbey, F. Mahmoudi, O. Stal, and T. Stefaniak, *Eur. Phys. J. C* **78**, 182 (2018).
- [112] A. G. Akeroyd, *Nucl. Phys.* **B544**, 557 (1999).
- [113] V. Khachatryan *et al.* (CMS Collaboration), *J. High Energy Phys.* **11** (2015) 018.
- [114] G. Aad *et al.* (ATLAS Collaboration), *Eur. Phys. J. C* **73**, 2465 (2013).
- [115] G. Aad *et al.* (ATLAS Collaboration), *J. High Energy Phys.* **03** (2015) 088.
- [116] V. Khachatryan *et al.* (CMS Collaboration), *J. High Energy Phys.* **12** (2015) 178.
- [117] G. Aad *et al.* (ATLAS Collaboration), *Eur. Phys. J. C* **76**, 6 (2016).
- [118] V. Khachatryan *et al.* (CMS Collaboration), *Eur. Phys. J. C* **75**, 212 (2015).
- [119] M. Bauer, M. Klassen, and V. Tenorth, *J. High Energy Phys.* **07** (2018) 107.
- [120] Y. Amhis *et al.* (HFLAV Collaboration), *Eur. Phys. J. C* **77**, 895 (2017).
- [121] M. Misiak and M. Steinhauser, *Eur. Phys. J. C* **77**, 201 (2017).
- [122] S. Karmakar and S. Rakshit, *Phys. Rev. D* **100**, 055016 (2019).
- [123] P. Achard *et al.* (L3 Collaboration), *Phys. Lett. B* **517**, 75 (2001).
- [124] A. Falkowski, D. M. Straub, and A. Vicente, *J. High Energy Phys.* **05** (2014) 092.
- [125] P. Gondolo and G. Gelmini, *Nucl. Phys.* **B360**, 145 (1991).
- [126] A. Semenov, *Comput. Phys. Commun.* **180**, 431 (2009).
- [127] G. Belanger, F. Boudjema, A. Pukhov, and A. Semenov, *Comput. Phys. Commun.* **149**, 103 (2002).
- [128] J. Billard, L. Strigari, and E. Figueroa-Feliciano, *Phys. Rev. D* **89**, 023524 (2014).
- [129] A. Belyaev, N. D. Christensen, and A. Pukhov, *Comput. Phys. Commun.* **184**, 1729 (2013).
- [130] T. Sjostrand, S. Mrenna, and P. Z. Skands, *J. High Energy Phys.* **05** (2006) 026.
- [131] J. Alwall, M. Herquet, F. Maltoni, O. Mattelaer, and T. Stelzer, *J. High Energy Phys.* **06** (2011) 128.
- [132] J. Alwall, R. Frederix, S. Frixione, V. Hirschi, F. Maltoni, O. Mattelaer, H. S. Shao, T. Stelzer, P. Torrielli, and M. Zaro, *J. High Energy Phys.* **07** (2014) 079.
- [133] R. Placakyte, in *Proceedings of the 31st International Conference on Physics in Collisions (PIC 2011): Vancouver, Canada* (2011), arXiv:1111.5452.
- [134] C. L. Wainwright, *Comput. Phys. Commun.* **183**, 2006 (2012).
- [135] S. R. Coleman and E. J. Weinberg, *Phys. Rev. D* **7**, 1888 (1973).
- [136] P. B. Arnold and O. Espinosa, *Phys. Rev. D* **47**, 3546 (1993); **50**, 6662(E) (1994).
- [137] F. P. Huang and J.-H. Yu, *Phys. Rev. D* **98**, 095022 (2018).
- [138] N. Blinov, S. Profumo, and T. Stefaniak, *J. Cosmol. Astropart. Phys.* **07** (2015) 028.
- [139] T. Vieu, A. P. Morais, and R. Pasechnik, *J. Cosmol. Astropart. Phys.* **07** (2018) 014.
- [140] G. Gil, P. Chankowski, and M. Krawczyk, *Phys. Lett. B* **717**, 396 (2012).
- [141] A. D. Linde, *Nucl. Phys.* **B216**, 421 (1983); **B223**, 544(E) (1983).
- [142] R. Jinno and M. Takimoto, *Phys. Rev. D* **95**, 024009 (2017).
- [143] R. Jinno and M. Takimoto, *J. Cosmol. Astropart. Phys.* **01** (2019) 060.
- [144] J. Kozaczuk, *J. High Energy Phys.* **10** (2015) 135.
- [145] P. J. Steinhardt, *Phys. Rev. D* **25**, 2074 (1982).
- [146] J. Ellis, M. Lewicki, and J. M. No, *J. Cosmol. Astropart. Phys.* **04** (2019) 003.
- [147] J. Ellis, M. Lewicki, J. M. No, and V. Vaskonen, *J. Cosmol. Astropart. Phys.* **06** (2019) 024.
- [148] T. Alanne, T. Hogle, M. Platscher, and K. Schmitz, arXiv:1909.11356.
- [149] E. Thrane and J. D. Romano, *Phys. Rev. D* **88**, 124032 (2013).
- [150] P. S. B. Dev, F. Ferrer, Y. Zhang, and Y. Zhang, *J. Cosmol. Astropart. Phys.* **11** (2019) 006.
- [151] V. Khachatryan *et al.* (CMS Collaboration), *J. High Energy Phys.* **02** (2017) 135.